

3D PIC Simulations for Relativistic Jets with a Toroidal Magnetic Field

Athina Meli,^{1,2,*} Kenichi Nishikawa,³ Christoph Köhn,⁴ Ioana Duțan,⁵ Yosuke Mizuno,^{6,7}
Oleh Kobzar,⁸ Nicholas MacDonald,⁹ José L. Gómez¹⁰ and Kouichi Hirotani¹¹

¹College of Science and Technology, North Carolina A&T State University, North Carolina, NC 27411, USA

²Space Sciences & Technologies for Astrophysics Research (STAR) Institute Université de Liège, Sart Tilman, 4000 Liège, Belgium

³Department of Physics, Chemistry and Mathematics, Alabama A&M University, Normal, AL 35762, USA

⁴Technical University of Denmark, National Space Institute (DTU Space), Elektrovej 328, 2800 Kgs Lyngby, Denmark

⁵Institute of Space Science, Atomistilor 409, RO-077125 Bucharest-Măgurele, Romania

⁶Institute for Theoretical Physics, Goethe University, D-60438 Frankfurt am Main, Germany

⁷Tsung-Dao Lee Institute, Shanghai Jiao Tong University, Shanghai, 200240, China

⁸Faculty of Materials Engineering and Physics, Cracow University of Technology, PL-30084 Krakow, Poland

⁹Max-Planck-Institut für Radioastronomie, Auf dem Hügel 69, D-53121 Bonn, Germany

¹⁰Instituto de Astrofísica de Andalucía, CSIC, Apartado 3004, 18080 Granada, Spain

¹¹Taiwan Institute of Astronomy and Astrophysics, Academia Sinica, Taipei 10617, Taiwan, Republic of China

Accepted Received ; in original form

ABSTRACT

We have investigated how kinetic instabilities such as the Weibel instability (WI), the mushroom instability (MI), and the kinetic Kelvin-Helmholtz instability (kKHI) are excited in jets without and with a toroidal magnetic field, and how such instabilities contribute to particle acceleration. In this work we use a new jet injection scheme where an electric current is self-consistently generated at the jet orifice by the jet particles which produce the toroidal magnetic field. We perform five different simulations for a sufficiently long time to examine the non-linear effects of the jet evolution. We inject unmagnetized e^+ and $e^- - p^+$ ($mp/me = 1836$), as well as magnetized e^+ and $e^- - i^+$ ($mi/me = 4$) jets with a top-hat jet density profile into an unmagnetized ambient plasmas of the same species. We show that WI, MI, and kKHI excited at the linear stage, generate a non-oscillatory x-component of the electric field accelerating and decelerating electrons. We find that the two different jet compositions (e^+ and $e^- - i^+$) display different instability modes respectively. Moreover, the magnetic field in the non-linear stage generated by different instabilities is dissipated and reorganized into new topologies. A 3D magnetic field topology depiction indicates possible reconnection sites in the non-linear stage where the particles are significantly accelerated by the dissipation of the magnetic field associated to a possible reconnection event.

Key words: acceleration of particles, relativistic processes, instabilities, shock waves, galaxies: jets

1 INTRODUCTION

Relativistic astrophysical jets are ubiquitous in astrophysical systems. Most collimated relativistic jets extend between several thousands up to millions of parsecs (e.g., Blandford et al. 2019) and have been observationally associated with the activity of central black holes in Active Galactic Nuclei (AGN, e.g. EHT Collaboration 2019; Kim et al. 2020). It is also theorized that relativistic jets may also occur in Gamma-ray Bursts (GRBs) (e.g. Ruiz et al. 2018). The formation and powering of these astrophysical jets are highly complex phenomena involving relativistic plasmas and twisted magnetic fields which are organized in such a manner as to ultimately launch an outflow from a central compact source.

For almost two decades, Particle-in-Cell (PIC) models have been used to study unmagnetized and magnetized relativistic jets that in-

teract with the interstellar medium. These investigations have offered tremendous insight into the instabilities, turbulence, and shocks that can develop in the out-flowing plasma, leading to particle acceleration and the production of nonthermal radiation (e.g., Silva et al. 2013; Nishikawa et al. 2003; Jaroschek et al. 2005; Spitkovsky 2008a,b; Dieckmann et al. 2008; Nishikawa et al. 2009; Giannios et al. 2009; de Gouveia Dal Pino et al. 2010; Uzdensky 2011; Granot 2012; McKinney & Uzdensky 2012; Sironi et al. 2013, 2015; Ardaneh et al. 2016; Kadowaki et al. 2018, 2019; Christie et al. 2019; Fowler et al. 2019).

Relativistic jets interact with the plasma environment of an astrophysical source and subsequently instabilities occur which are responsible for the acceleration of particles (e.g., Nishikawa et al. 2021). Beam-plasma instabilities are a key physical process in many astrophysical phenomena, therefore extensive investigations of various instabilities have been performed (e.g., Bret 2009; Bret et al. 2010). In the context of this work we discuss possible instabilities

*E-mail: ameli@ncat.edu

in the simulation system used and we note that the filamentation instability and the two-stream instability are not the same instability. The non-resonant filamentation instability is mostly magnetic and drives waves with wavevectors that are almost perpendicular to the plasma flow direction. The current filaments are seen in the early linear stage as shown in the movies provided, and in particular in the unmagnetized cases. The two-stream instability or Buneman instability is a resonant electrostatic instability, which triggers the growth of wavevectors that are almost parallel to the plasma flow direction. Both instabilities have growth rates that scale quite differently with the Lorentz factor of the flow velocity (e.g., Bret et al. 2010). For the magnetized cases, different modes such as oblique and Bell's ones can be excited (e.g., Bret 2009; Bret et al. 2010). On that matter further studies are necessary to recognize these excited modes in the linear stage. In the present work we use the term "Weibel instability" (WI) for possible filamentation instability and other modes. The WI results in particle acceleration (e.g., Silva et al. 2013; Nishikawa et al. 2003; Jaroschek et al. 2005; Spitkovsky 2008a,b; Dieckmann et al. 2008; Nishikawa et al. 2009).

Other instabilities such as the kinetic Kelvin-Helmholtz (kKHI) and the mushroom instability (MI) are driven by the velocity-shear at the boundary between the jet and the ambient medium in 2D and 3D systems without external magnetic fields (e.g., Alves et al. 2012; Nishikawa et al. 2013; Liang et al. 2013a,b; Grismayer et al. 2013; Nishikawa et al. 2014; Alves et al. 2015). It should be noted here that the kKHI is generated along the jet direction, in contrast to the MI, which is excited in the direction perpendicular to the jet and their growth rates depend on the relative velocity of the particles (e.g., Alves et al. 2012, 2015). For an e^\pm jet (e.g., Liang et al. 2013a,b; Nishikawa et al. 2014; Alves et al. 2015), both kKHI and MI generate an AC magnetic field whilst an electron-ion jet (e.g., Alves et al. 2012; Nishikawa et al. 2014) generates a DC magnetic field. For the case of $m_i/m_e = 4$ the growth rate of the MI is reduced comparing to the case of $m_p/m_e = 1836$, and a quasi-AC electric field is generated with slightly accelerated jet ions.

PIC simulation studies of the evolution of cylindrical jets without and with a helical magnetic-field topology have been performed in the past (e.g., Nishikawa et al. 2016a,b, 2019; Nishikawa et al. 2021). The present investigation focuses on the nature of particle acceleration in these relativistic plasma flows with a toroidal magnetic field.

An additional possible mechanism of particle acceleration in jets is magnetic reconnection. In this process the magnetic topology is rearranged and the magnetic energy is converted into thermal and kinetic particle energy. Magnetic reconnection is observed in solar and planetary magnetospheric plasmas. It is also often assumed to be an important mechanism of particle acceleration in extragalactic environments such as AGN (active galactic nuclei) and GRB (gamma-ray bursts) jets (e.g., Drenkhahn & Spruit 2002; de Gouveia Dal Pino & Lazarian 2005; Uzdensky 2011; Zhang & Yan 2011; Granot 2012; McKinney & Uzdensky 2012; Giannios 2010; Komissarov 2012; Giannios 2013; Sironi et al. 2015; de Gouveia Dal Pino et al. 2018; Kadowaki et al. 2018, 2019; Christie et al. 2019; Fowler et al. 2019; Zhang 2018).

Magnetic reconnection has commonly been studied with PIC simulations using the so-called Harris model in a slab geometry. It was observed to produce a significant particle acceleration (e.g., Zenitani & Hoshino 2005; Oka et al. 2008; Daughton 2011; Kagan et al. 2013; Wendel et al. 2013; Karimabadi et al. 2014; Sironi & Spitkovsky 2014; Guo et al. 2015, 2016a,b). These studies however cannot be applied directly to astrophysical relativistic jets, since observations (Hawley et al. 2015; Gabuzda 2019), as well as MHD

modelling (Tchekhovskoy 2015), suggest that the magnetic-field topology is pre-dominantly helical; i.e., it consists of toroidal and poloidal magnetic field components.

Global 3D PIC modeling of relativistic jets allows for a self-consistent investigation of the complex kinetic processes occurring in the jet and the surrounding medium. These processes can reveal electron-scale short-wavelength instabilities, their saturation and associated phenomena. Such studies have been first performed for unmagnetized jets (Nishikawa et al. 2016a). PIC simulations of relativistic jets containing helical magnetic fields were, for the first time, presented by Nishikawa et al. (2016b). These initial studies addressed the early, linear growth of kinetic instabilities in the electron-ion and electron-positron jets. However, such simulations were limited by the size of the computational box.

The present study involves a much larger jet radius and longer simulation times than previous works (e.g., Nishikawa et al. 2016a,b, 2017), allowing for a non-linear evolution of the jets with a toroidal magnetic field. It is designed to address the following key questions:

- (i) How does a toroidal magnetic field affect the growth of kKHI, MI, and WI within the jet and in the jet-ambient plasma boundary?
- (ii) How do jets composed of electrons and positrons and jets composed of electrons and ions evolve in the presence of a large-scale toroidal magnetic field?
- (iii) How and where are particles accelerated in jets with different plasma compositions?

Since the magnetic field structure and particle composition of relativistic jets is still not well understood, this systematic study of $e^- - i^+$ ($e^- - p^+$) and e^\pm jets containing a toroidal field helps to provide an advanced and detailed understanding of the magnetic field evolution, the generation of instabilities, possible reconnection events, and the particle acceleration applicable in the environments of AGN and GRB jets. It is important to note that the differences in the magnetic field morphologies between jets composed of $e^- - i^+$ ($e^- - p^+$) and e^\pm could leave significant imprints on the polarized emission from AGN jets and GRBs. Particularly, circular polarization (measured as the Stokes parameter V) in the continuum radio emission from AGN jets provides a powerful diagnostic tool of magnetic structures and particle composition because, unlike linear polarization, circular polarization is expected to remain almost completely unmodified by external screens (e.g., O'Sullivan et al. 2013; MacDonald & Nishikawa 2021).

It is important to note, as discussed in Nishikawa et al. (2020) for $e^- - p^+$ jets, that our simulations do not address the large-scale plasma flows of macroscopic parsec-scale jets studied by relativistic magnetohydrodynamic (RMHD) simulations. Instead they explore the relevant kinetic-scale physics within relativistic jet plasmas, which cannot be studied with RMHD simulations. Although in PIC simulations we need to resolve the electron Debye length, the simulation sizes which are feasible at the present time are limited (for more details see MacDonald & Nishikawa (2021)). Our study, therefore, is complementary to RMHD models and yields important insights into the kinetic processes at work in relativistic astrophysical jets (see also Nishikawa et al. 2020, 2021; Meli & Nishikawa 2021).

This paper is organized as follows: After we describe the simulation set-up in Section 2, the main differences between electron-positron and electron-ion (electron-proton) jets are shown at the linear stage and at the fully developed non-linear stage in Section 3. In particular, we discuss the kinetic instabilities in the linear and non-linear stage in subsection 3.1. In subsection 3.2 we present results about acceleration and discuss the patterns of electron acceleration and deceleration in comparison with the structure of the electromag-

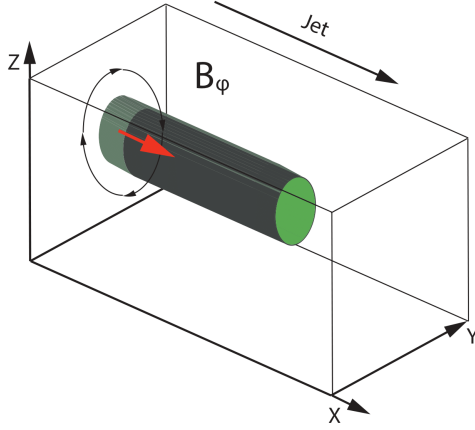


Figure 1. A schematic of the jet injection scheme with a toroidal magnetic field (B_ϕ). The jet electrons and positrons/ions/protons are injected such that a current (indicated by the red arrow) is generated to support the toroidal magnetic field.

netic field. We show the three-dimensional magnetic field evolution in subsection 3.4. Lastly, in subsection 3.4 we present results about the role of the non-linear stage, the instabilities growth and their role to consequent acceleration. In Section 4, we summarize and discuss our conclusions.

2 SIMULATION SET-UP

Our 3D PIC code is a modified version of the relativistic electro-magnetic PIC code TRISTAN (Buneman 1993) with MPI-based parallelization (Niemiec et al. 2008; Nishikawa et al. 2009). The numerical grid is set to $(L_x, L_y, L_z) = (1285\Delta, 789\Delta, 789\Delta)$ and is twice as long as that in our previous simulation studies (Nishikawa et al. 2016b, 2017, 2019). Here $\Delta = 1$ is the size of an individual grid cell. Open boundaries are used on the surfaces at $x/\Delta = 0$ and $x/\Delta = 1285$, whilst periodic boundary conditions are implemented along the transverse directions y and z . Since the jet is located in the center of the simulation box far from the boundaries, the effect of periodic boundaries is negligible.

2.1 New jet injection scheme and simulation parameters

In this work, we use a new jet injection scheme. The system needs to be neutral and in equilibrium, therefore we fill the ambient plasma with electrons and positrons (ions $m_i/m_e = 4$) at the same positions randomly, and then we inject jet particles (electrons, positrons and ions). All particles are self-consistently pushed in the system. We inject a cylindrical jet into the ambient plasma which is at rest. The jet then propagates in the x -direction, with a toroidal magnetic field (Eq. 2), as schematically shown in Fig. 1. The jet is injected at $x = 100\Delta$ in the center of the $y - z$ plane at $(y_{jc} = 381\Delta, z_{jc} = 381\Delta)$, and propagates in the x -direction. Its radial width in cylindrical coordinates is $r_{jet} = 100\Delta$. In this study, we apply only a toroidal magnetic field

$$\vec{B}_\phi(r) = \frac{B_0(r/a)}{[1 + (r/a)^2]}. \quad (1)$$

The poloidal field component, B_x (e.g., Nishikawa et al. 2020), is not included. B_ϕ has a peak amplitude at $r = a$ where a is the

characteristic radius. In Cartesian coordinates, the corresponding field components, B_y and B_z , are calculated as

$$B_y(y, z) = \frac{(z - z_{jc})B_0}{a[1 + (r/a)^2]}, \quad B_z(y, z) = -\frac{(y - y_{jc})B_0}{a[1 + (r/a)^2]}. \quad (2)$$

Equation (2) describes the magnetic field of left-handed polarity for positive B_0 . In this study we assume $a = 50\Delta$.

With respect to the electric field and its associated current, initially there is no current, and so $\partial E/\partial t = \text{curl } \mathbf{B} = \mathbf{J}$. Since we need to generate a current based on the applied toroidal magnetic field B_ϕ as defined above, we apply a current

$$J_x = \frac{1}{r} \frac{\partial(r/a)B_0/[1 + (r/a)^2]}{\partial r} = \frac{2B_0}{a[1 + (r/a)^2]^2}. \quad (3)$$

For the toroidal magnetic field outside of the jet we multiply Equation (2) with a damping function:

$$\Theta(r - r_{jet}) = \frac{r_{jet}}{r}, \quad \text{where } r > r_{jet}. \quad (4)$$

Since the current is situated only inside the jet, the toroidal magnetic field outside the jet decays sharply, which help us utilise a smaller simulation box.

We assume a top-hat density profile for both jets. Although the shape of a real jet is far more complex, the present results are the first step in a series of advanced numerical investigations including an implementation of a Gaussian (Lorentzian) (non top-hat) profile, which is closer to jet density profiles generated by General RMHD (GRPIC) simulations (e.g., Nishikawa et al. 2021).

First, we calculate the velocities of the jet particles based on $\mathbf{J}(r) = \nabla \times \mathbf{B}$ in the jet frame using Eq. (3). After applying a Lorentz transformation we get the velocity of the jet electrons ($v'_{e,x}$) and ions ($v'_{i,x}$) in the jet frame:

$$v'_{e,x} = \frac{1}{e n_e} \frac{m_i}{m_i + m_e} \frac{2B_0}{a[1 + (r/a)^2]^2} \\ v'_{i,x} = -\frac{1}{e n_e} \frac{m_e}{m_i + m_e} \frac{2B_0}{a[1 + (r/a)^2]^2} \quad (5)$$

where n_e : jet electron density, e : electron charge, m_e : electron mass, and m_i : ion mass.

We now transform the jet-frame drift velocities back to the simulation frame. The relative velocity between the frames is $v_j/c = \beta_0 = \sqrt{1 - \Gamma_0^{-2}} \approx 0.9977753$ ($c = 1$). Based on the Lorentz transformation $v_{e,x}$ in the simulation frame:

$$v_{e,x} = \frac{v'_{e,x} + \beta_0 c}{1 + \beta_0 \frac{v'_{e,x}}{c}} \quad (6)$$

Then the velocities of the jet particles are Lorentz-transformed to the simulation frame. In the simulation frame the jet electrons propagate faster than positrons (ions, protons), which generates a negative current in the jet (clockwise as viewed from the jet head). In order to sustain the current in the jet, a toroidal magnetic field is gradually applied at the jet orifice using $B(t) = B_0 * 0.5 * (\tanh(t_{\text{ramp}} - 3.0) + 1.0)$ where $t_{\text{ramp}} = \text{float}(nstep) * 0.012$ ($nstep$: simulation step), located at $x/\Delta = 100 - 102$, and a motional electric field is established, $\mathbf{E}_{\text{mot}} = -\mathbf{v}_j \times \mathbf{B}$. Here, $\mathbf{v}_j = v_{j,x} \hat{\mathbf{x}}$, where $v_{j,x}$ is the x -component of the jet velocity. In this way one avoids non-linear effects emerging from the constantly applied magnetic field in the simulation frame where unnatural banding and currents in the centre of the jet might occur (e.g., Nishikawa et al. 2020).

In these simulations, the jet Lorentz factor is set to $\gamma_{jt} = 15$.

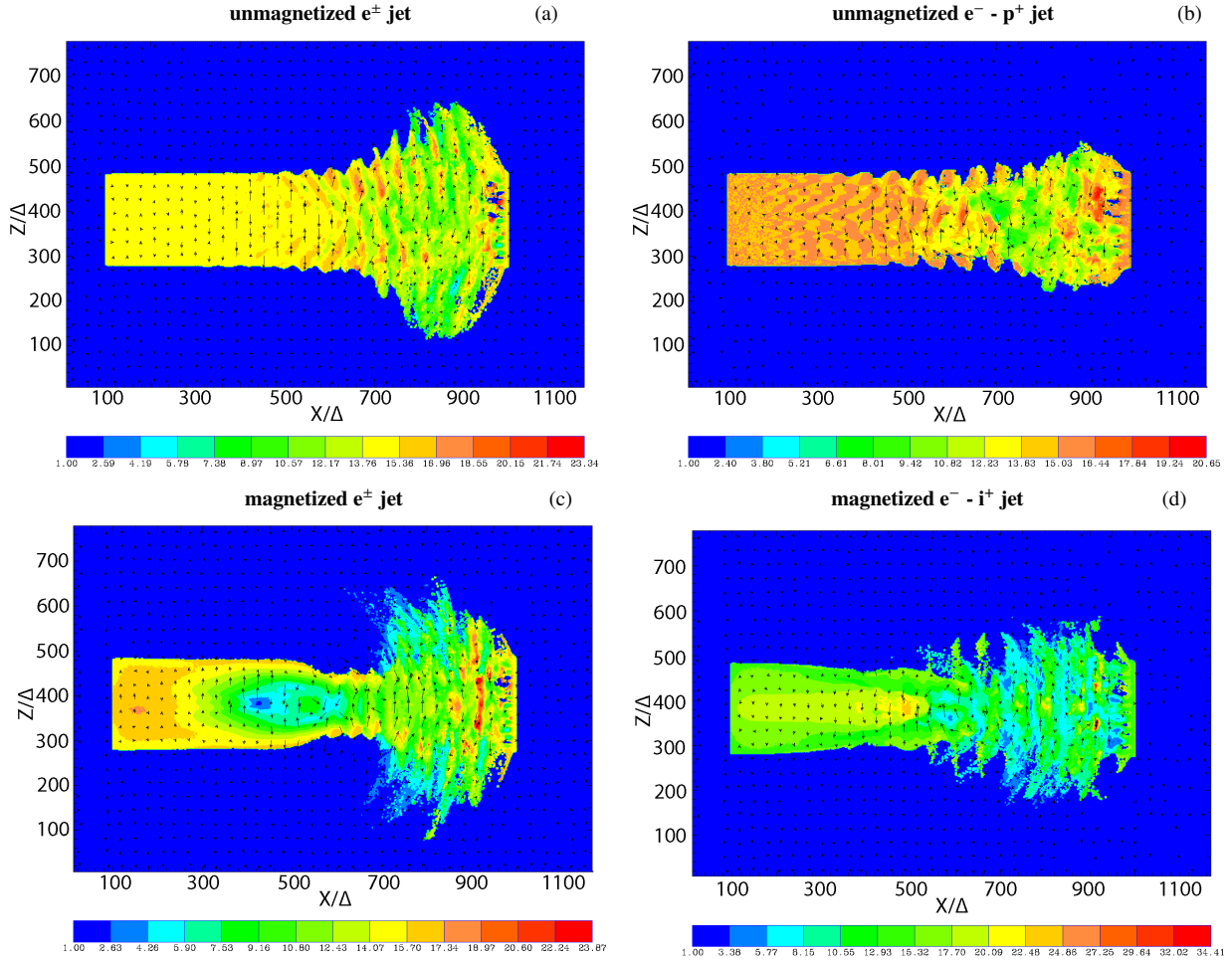


Figure 2. Color maps of the Lorentz factor of the jet electrons at $y/\Delta = 381$ (shown below the panels) for e^\pm jets (left panels) and the $e^- - p^+$ jet (b) the $e^- - i^+$ jet (d) with $r_{\text{jet}} = 100\Delta$ at time $t = 900 \omega_{\text{pe}}^{-1}$. Panels (a) and (b) show unmagnetized jets and panels (c) and (d) the jets with the toroidal magnetic field. Black arrows show the in-plane magnetic field (B_x, B_z). The maximum is (a): 23.34, (b): 20.65, (c): 23.87, and (d): 34.41. The minimum is 1.0 for all panels.

We perform simulations for both unmagnetized and magnetized jets, while keeping the ambient medium unmagnetized. In the case of a magnetized jet, the jet is initially moderately magnetized, that is the jet's magnetic-field amplitude $B_0 = 0.5$, corresponds to a plasma magnetization $\sigma = B_0^2 / (n_e m_e \gamma_{\text{jt}} c^2) = 1.73 \times 10^{-2}$, where c is the speed of light, m_e is the electron rest mass and n_e the electron density. In order to investigate the non-linear stage of the jet's evolution, we follow the jet for a sufficiently long time of $t_{\text{max}} = 900 \omega_{\text{pe}}^{-1}$, where $\omega_{\text{pe}} = (e^2 n_{\text{amb}} / (\epsilon_0 m_e))^{1/2}$ is the electron plasma frequency.

Both the jet and the ambient plasma are composed of electrons and ions (protons) or of electrons and positrons. The initial number densities measured in the simulation frame are $n_{\text{jt}} = 8$ and $n_{\text{amb}} = 12$ in the jet and in the ambient plasma, respectively. The Debye length for the ambient electrons is $\lambda_D = 0.5\Delta$ and the electron skin depth is $\lambda_{\text{se}} = c/\omega_{\text{pe}} = 10.0\Delta$. The thermal speed of jet electrons is $v_{\text{jt,th,e}} = 0.014c$ in the jet frame whilst in the ambient plasma it is $v_{\text{am,th,e}} = 0.05c$. The thermal speed of ions is smaller by a factor of $(m_p/m_e)^{1/2} \approx 42$ for unmagnetized (magnetized) $e^- - p^+$ jet, and $(m_i/m_e)^{1/2} \approx 2$ for magnetized $e^- - i^+$ jet. It should be noted that for the unmagnetized $e^- - p^+$ jet the large mass ratio contributes to a stronger growth of the MI. For that reason we reduce the mass ratio to control the growth of MI, that is from $m_p/m_e = 1836$ to $m_i/m_e = 4$. Although in most PIC simulation studies mass ratios of

16, 25 or larger are used (e.g., [Bret & Dieckmann 2010](#)), in this study we chose to use a smaller mass ratio ($m_i/m_e = 4$). This is because we need to avoid anomalous effects (when using $m_p/m_e = 1836$) in the evolution of the relativistic jet (which is not shown), given the small radius we apply in the present simulations. At the same time with this small mass ratio of ion-to-electron, we can compare the evolution differences to a pair jet.

3 RESULTS OF SIMULATIONS OF A JET WITH A TOROIDAL MAGNETIC FIELD

We present simulation results for e^\pm and $e^- - i^+$ jets with a toroidal magnetic field, applying a new and improved jet injection scheme. We are in particular interested in the differences in the dynamical behavior of the jets of different plasma compositions and in the way these jets interact with the surrounding environment. In order to give an overview of how the toroidal magnetic field affects the evolution of the jet, in Figs. 2-5 we present simulation results for jets with a toroidal field (shown in the lower panels of each figure) and compare them to the results obtained for an unmagnetized jet.

Figure 2 presents the global jet structure and shows the Lorentz factor of the jet electrons for an e^\pm (a, c), an $e^- - p^+$ (b), and an $e^- - i^+$ (d) jet. In all panels the magnetic field direction in the $x -$

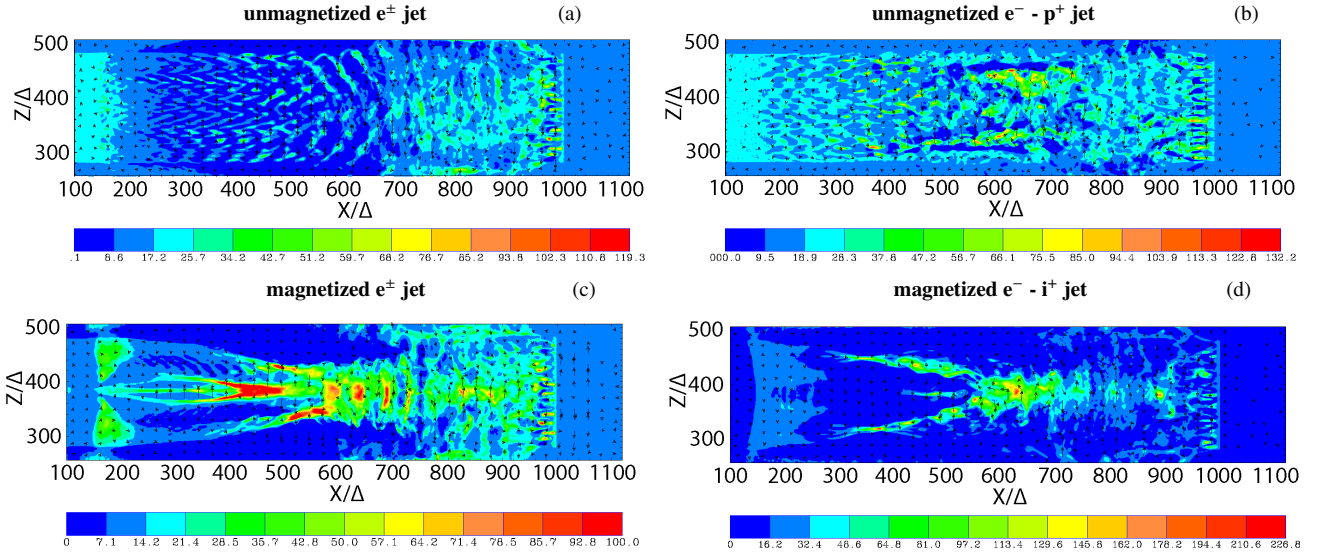


Figure 3. Color maps of the jet electron density with black arrows depicting the magnetic field components in the $x - z$ plane, at $t = 900 \omega_{pe}^{-1}$. As in Fig. 2, left panels show results for e^{\pm} jets and the right panels for $e^{-} - p^{+}$ jets. Upper panels (a) and (b) show unmagnetized jets and lower panels (c) and (d) jets with a toroidal magnetic field. Note that the maps display the jet structures in a region of the computational box, $250 < x/\Delta < 500$, that fully encompasses the injected jet with $r_{jet} = 100\Delta$. The jet electron density at injection is $n_{jt} = 8$. The maximum is (a): 119.3, (b): 132.2, (c): 100.0, and (d): 226.8. The minimum is essentially 0.0 for all panels.

z plane is indicated by the black arrows. It is noted that the applied toroidal magnetic field in the $x - z$ plane should be zero but at the center of the jet (as shown the regions $(x/\Delta < 250)$, the x and z components are generated by the excited instabilities (WI, MI, and kKHI). For the e^{\pm} jets, the structures seen at the boundary between the jet and the ambient plasma at $400 < x/\Delta < 1000$ show the excitation and development of kKHI and MI, where the MI represents the transverse component/dynamics of the kKHI. It is interesting that at $600 < x/\Delta < 700$ in panel c) one can see at an early stage, a central reversal of the magnetic field with an associated deceleration of the flow, and then a tight “bottle-neck” form, featuring a strong jet collimation trend. This strong collimation occurs due to the slender jet and an excited strong MI growth. This collimation of jet electrons is also seen in Fig. 3c. After the dissipation of the magnetic field around $x/\Delta = 750$ (see Fig. 4), the disruption around the location, where the non-linear stage starts, is evident for both the unmagnetized and magnetized e^{\pm} jets. Especially for the magnetized $e^{-} - p^{+}$ jet, a disruption and a reversal of the magnetic field occurs at earlier stages, which is not shown in this report, since the drastic expansion of jet electrons outside the jet is caused by the extremely small jet radius. We chose to re-ran the simulation with a mass ratio ($m_i/m_e = 4$) which shows a much weaker growth of MI, as we explained in Section 2. In the magnetized jet cases we also see a radial expansion, forming spikes with a simultaneous stratification of the electric field generated by the kKHI. It seems that the jet electrons are radially pushed as a main result of the excited instabilities (MI and kKHI) within the jet.

For the simulations of the unmagnetized $e^{-} - p^{+}$ jet case, the jet electrons remain highly energetic for longer within the jet and before the development of the non-linear stages, where some deceleration with collimation is seen. We further discern that at the non-linear stage the jet electrons are expanded outside and become ‘diluted’, which in turn deduces the average Lorentz factor. Longer simulations will provide further insights about the important non-linear stage of the jet evolution. We further discuss the particle Lorentz factor distributions in the jets in Section 3.2. In typical hydrodynamic simulations, the jets are characterized by a channel with a relativistic

outflow, which is separated from the surrounding materials by cocoons (Bromberg et al. 2011). In our simulations, the jet particles are injected into the ambient medium. Nevertheless, the jet particles and the ambient ones mix with each other only at the edge of the jet where the sheath instabilities take place. When we represent the plasma parameters for the jet, e.g., the Lorentz factor, we pick up only the jet particles from simulations. In Fig. 2, the 2D representation of the Lorentz factor of the jet particles shows the formation of a Mach-like cone, which, however, is not well developed as in the case of hydrodynamic simulations. One of the reasons for this shortcoming might be the fact that our simulations do not run long enough to generate a well-defined shock. In future work, we plan to use other setups for the jet density profile to be able to compare our results with hydrodynamic jet simulations. The PIC simulation results by Ardaneh et al. (2016), for example, show some similar structure of the jet head and contact discontinuity in the jet plasma as for the hydrodynamic jets.

Figure 3 depicts the density of the jet electrons (ambient electrons excluded) for e^{\pm} jets (left column) and $e^{-} - p^{+}$ (b) and $e^{-} - i^{+}$ (d) jets (right column) at $t = 900 \omega_{pe}^{-1}$. We observe that the jet electron density structures fluctuate significantly between the simulated cases. This is due to the expected excited instabilities, whose growth depends on the plasma conditions which are different for the two jet compositions and magnetizations. We note that in the jets with toroidal magnetic fields the jet electrons are strongly collimated towards the center of (i) the pair jet in a region $550 \lesssim x/\Delta \lesssim 750$ (compare also with Fig. 2, and (ii) for the $e^{-} - i^{+}$ jet in a region $550 \lesssim x/\Delta \lesssim 850$, which is coincident with a stronger MI and kKHI excited in the presence of the toroidal field, as we also show below (Fig. 6).

Figure 4 shows the amplitude of B_y component with the arrows indicating the magnetic field components in the $x - z$ plane¹. For the unmagnetized cases with an initial magnetic field $B_0 = 0$, an

¹ Supplementary videos at [doi: 10.5281/zenodo.7017747](https://doi.org/10.5281/zenodo.7017747)

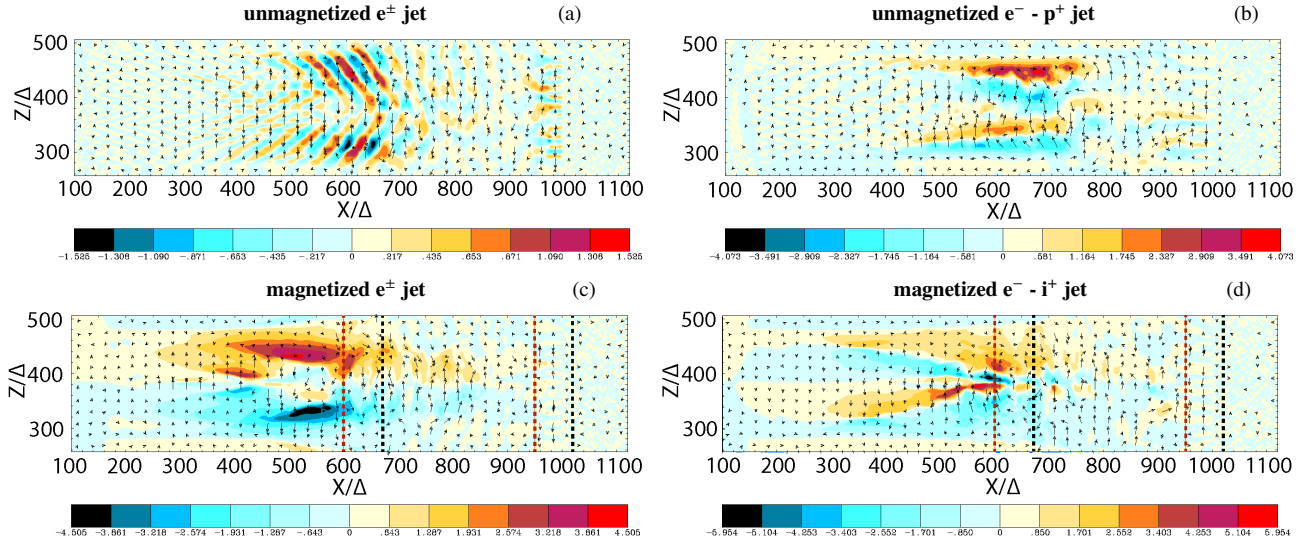


Figure 4. Color maps of the B_y magnetic field with arrows depicting the magnetic field components in the $x - z$ plane, at $t = 900 \omega_{pe}^{-1}$. Upper panels (a) and (b) show unmagnetized jets and lower panels (c) and (d) jets with a toroidal magnetic field. See Fig. 3. The squares with dashed lines indicate the areas plotted in the 3D displays in Fig. 11 (red) and Fig. 14 (blue). The maximum and minimum are (a): ± 1.525 , (b): ± 4.073 , (c): ± 4.505 and (d): ± 5.954 .

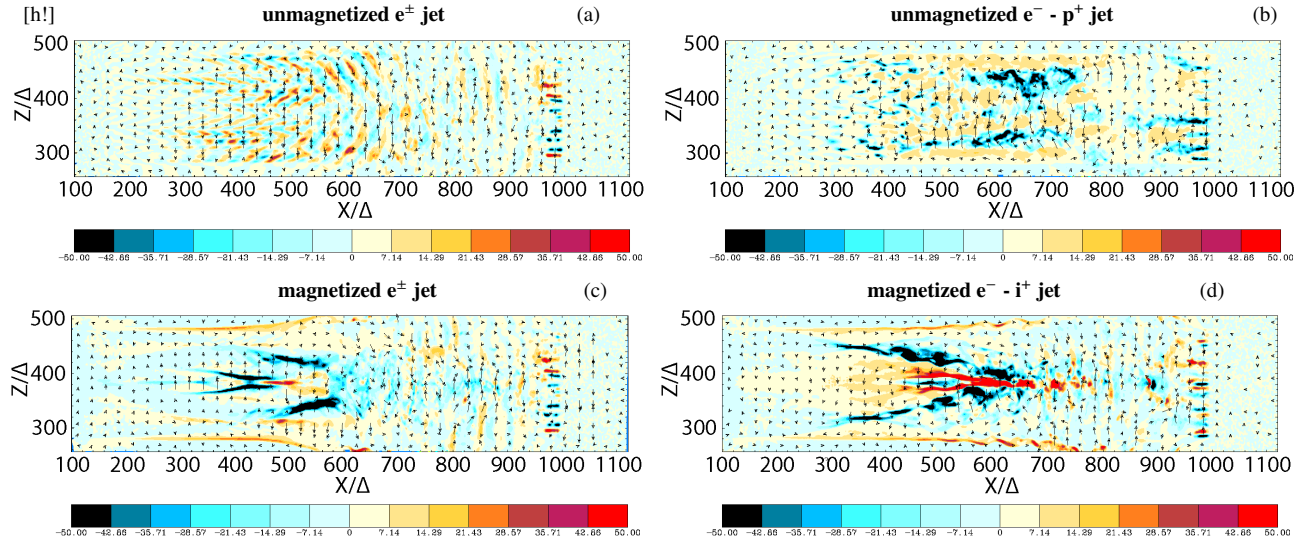


Figure 5. Color maps of the J_x component of the electric current with arrows showing the magnetic field components in the $x - z$ plane, at $t = 900 \omega_{pe}^{-1}$. See Fig. 3. In order to view the weaker current, the maximum and minimum values are set to ± 50 .

amplified magnetic field (B_y) is generated by the excited instabilities, as shown below. For the unmagnetized e^\pm jet, panel (a) shows that a two-stream instability (WI) is dominantly excited. For electron-proton ($e^- - p^+$) case, first, the two-streaming instability grows, later kKHI and MI grow at the jet boundary and they propagate into the jet center due to $m_p/m_e = 1836$. Consequently, Panel (b) shows the dominantly excited MI/rm (and kKHI) in the unmagnetized $e^- - p^+$ jet. For the magnetized jets, we apply $B_0 = 0.5$ initially at the jet orifice while B_y is measured in the same units. In the presence of the toroidal magnetic field for the e^\pm jet, we find a maximum value of $B_y = 4.505$ (Fig. 4c), which means that B_0 is amplified by a factor of 9.01 over the initial value. It is a factor of 2.95 stronger than magnetic fields in the unmagnetized e^\pm jet. The evident differences in the magnetic field structure in cases with and without the initial field,

indicate a significant impact of the toroidal field on the development of the kinetic instabilities. The same is true for the $e^- - i^+$ jet, in which the magnetic field amplification is comparably stronger and the field amplitudes reach $B/B_0 \approx 10.6$, a factor of 1.3 stronger compared to the unmagnetized $e^- - p^+$ jet case. As aforementioned, for the unmagnetized $e^- - p^+$ jet the large mass ratio contributes to a stronger growth of the MI, that is the reason we needed to reduce the mass ratio to control the growth of MI (from $m_p/m_e = 1836$ to $m_i/m_e = 4$). We note that for the e^\pm jet the magnetic field dissipates, i.e., becomes considerably weakened, at the jet region $x/\Delta \gtrsim 680$ and similarly for the $e^- - i^+$ jet the weakening occurs around $x/\Delta \gtrsim 700$. By comparing both magnetized jet species, at the non-linear stage close to $x/\Delta \gtrsim 950$, one discerns that for the electron-ion jet the B_y field almost dissipates and becomes disorganized (turbulent).

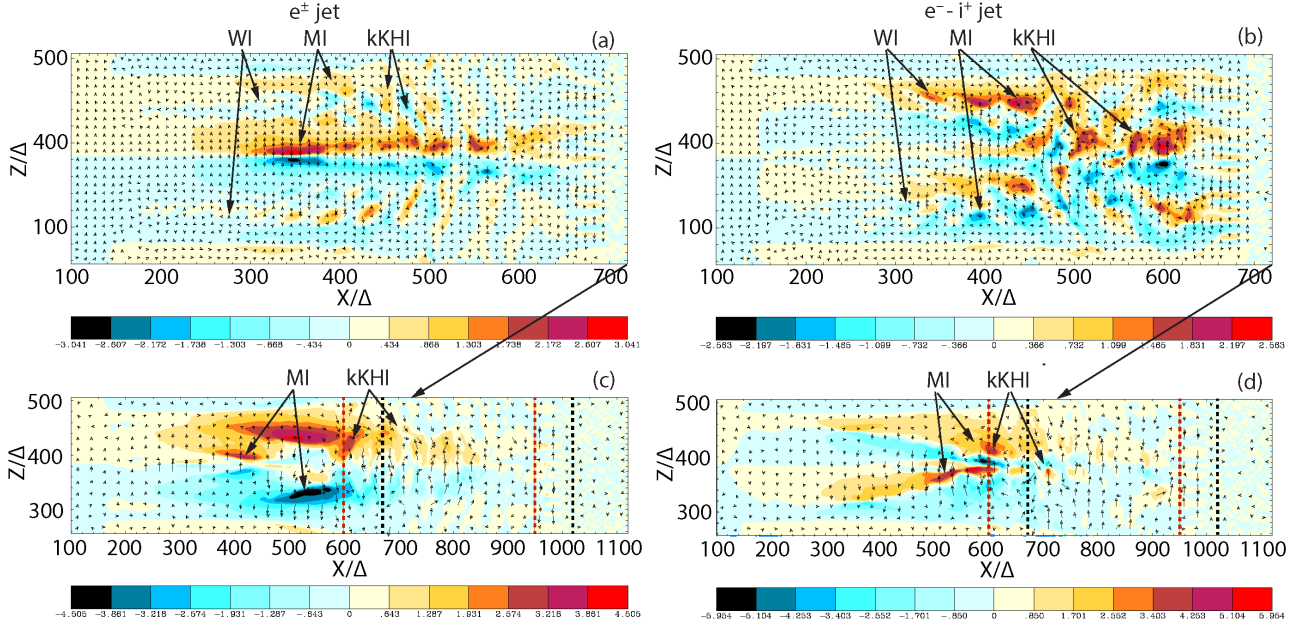


Figure 6. Color maps of the magnetic field amplitude B_y and arrows depicting the magnetic field components in the x - z plane, both at $t = 600 \omega_{pe}^{-1}$ (upper panels) and $900 \omega_{pe}^{-1}$ (lower panels), respectively. The jet is injected at $x = 100\Delta$ in the middle of the y - z plane and propagates in $+x$ -direction. Panels (a, c) are for an e^\pm plasma while panels (b, d) are for an $e^- - i^+$ composition. The peak amplitudes of B_y are (a) ± 3.041 , (b) ± 2.583 , (c) ± 4.505 and (d) ± 5.954 .

Figure 5 shows the current amplitude J_x and the magnetic field components (by arrows) in the x - z plane. For the magnetized pair jet the strong negative component $-J_x$ (blue) near the center of the jet (Fig. 5c), which is initially excited at the jet boundary moves into the center of the jet. The second outer MI mode is seen around $x/\Delta = 550$. These MI modes are modulated by the growth of a kKHI, in particular in the non-linear stage $x/\Delta > 700$ (see also in Fig. 6c). The thin elongated negative currents in Fig. 5c away from the central region of the jet, correspond to the outer MI mode as indicated in Fig. 6c. Moreover, the strong merged concentric positive current at the center of the jet for the magnetized $e^- - i^+$ jet (Fig. 5d) $x/\Delta > 600$, shows more prominently the merged MI mode which is further modulated by the growth of the kKHI $x/\Delta > 750$ (Fig. 6d, correspondingly). Comparing these two cases (Figs. 5c,d), the structures of excited MI modes are clearly different in the linear stage.

3.1 Kinetic instabilities in the linear and non-linear stage

Figure 6 shows the magnetic field component B_y in the x - z plane at $y/\Delta = 381$ with an in-plane magnetic field depicted with black arrows. Results for jets with toroidal magnetic fields are shown and the upper panels present the field structures in the linear regime at time $t = 600 \omega_{pe}^{-1}$ (Figs. 6a,b), whereas the lower panels depict the non-linear stage at time $t = 900 \omega_{pe}^{-1}$ (compare Figs. 6c,d). The pair jet is shown on the left column (a, c), and the $e^- - i^+$ jet on the right column (b, d).

For both magnetized jets (Figs. 6a,b), as expected, an WI is initially generated inside the jet. The wavelength of the WI is about $4\lambda_{se}$. One can see how residues of the WI remain at the jet head after $x/\Delta > 600$. This phenomenon was investigated (without the toroidal magnetic field) by Ardaneh et al. (2016). Specifically, at the jet head of the e^\pm jet, at $x/\Delta \approx 700$ an instability generates magnetic field filaments aligned with the jet propagation direction. Downstream along the jet

an oblique mode (slanted stripes) of the WI dominates, visible as consecutive concentrated magnetic fields between $x/\Delta \approx 280 - 630$ (Fig. 6a,b). Then, the MI and kKHI start to grow simultaneously in the same region of the jet at the jet-ambient medium boundary and across the jet, as seen in panel a). The excitation of the MI and the kKHI is merged with the WI, which results in slanted striped structures of the magnetic field in the e^\pm jet. Because the growth rates of MI and kKHI are similar, the excited modes propagate towards the jet center. For the $e^- - i^+$ jet the instabilities are stronger and more prominent, nevertheless they look rather similar to the e^\pm jet. Note that the wavelength of the kKHI mode is about $6\lambda_{se}$, whilst the wavelength of the MI mode is about $5\lambda_{se}$ along the jet radius (i.e., perpendicular to the jet axis).

Figure 6c shows the grown MI and kKHI in the non-linear stage at $x/\Delta > 700$, as indicated with the black arrow. We see here how the MI grows stronger and generates two dominant modes along the jet radius, the inner mode having larger amplitude. Simultaneously, the longitudinal kKHI wave modes modulate the magnetic field along the jet. For the $e^- - i^+$ jet, Figure 6b shows that the MI grows around $x/\Delta = 450$ dominantly, it propagates toward the jet center modulated by the kKHI modes already at the linear stage. The supplemental movie ² shows clearly the MI mode growth.

In the non-linear stage, in Figure 6d we find a strong B_y component excited by MI at $t = 900 \omega_{pe}^{-1}$ (at approximately $580 \lesssim x/\Delta \lesssim 620$). There is a magnetic field amplification in the non-linear stage, which can be attributed to the kKHI and MI which was similarly observed in the unmagnetized case of Nishikawa et al. (2016a) (see also Fig. 4b). Here the outer MI mode merges with the inner mode (Fig. 6d) closer to the jet center, where one sees comparatively the highly concentrated negative and then positive J_x current in Fig. 5d. That means that the magnetic field structure is pinched by the MI which is strongly modulated due to the growth of kKHI along the jet,

² MovieBy_pairJet.mp4 at doi: 10.5281/zenodo.7017747

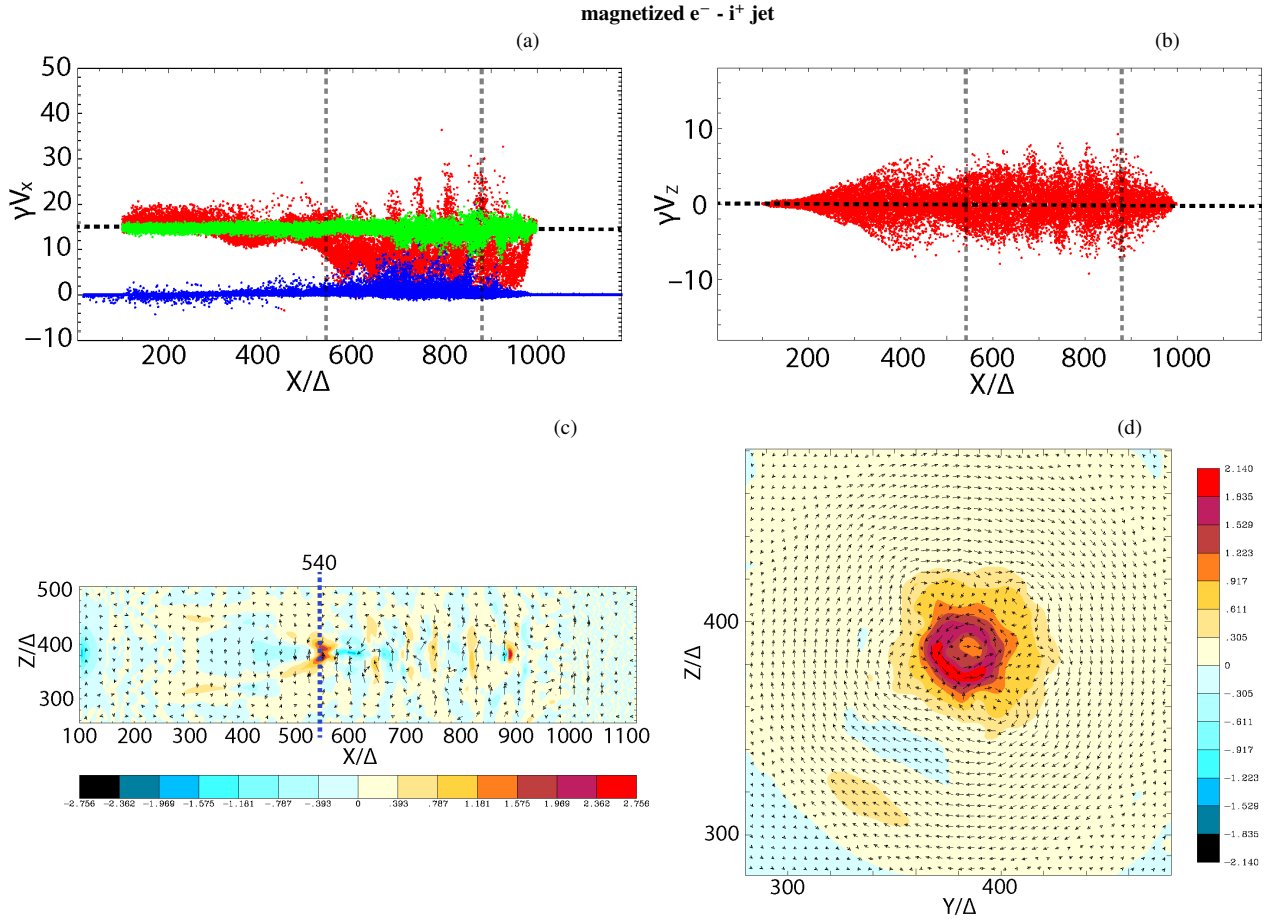


Figure 7. a) $x - \gamma v_x$ distribution of jet (red), and ambient (blue) electrons and jet ions (green) at $t = 900 \omega_{pe}^{-1}$, for an electron-ion jet. The initial $\gamma v_x = 15$ is marked with the horizontal dashed black line. b) $x - \gamma v_z$ distribution of jet electrons at $t = 900 \omega_{pe}^{-1}$. The initial $\gamma v_z = 0$ is marked with the horizontal dashed black line. c) The color-map of E_x in the $x - z$ plane at $y/\Delta = 381$, the dashed blue line is located at $x/\Delta = 540$. d) Color-map of E_x in the $y - z$ plane at $x/\Delta = 540$, marked by the vertical lines in panels (a), (b) and (c), arrows indicating $B_{y,z}$. The maxima and minima of E_x are (c): ± 2.754 and (d): ± 2.140 .

and demonstrates that the field collimation is caused primary by the pinching of the jet electrons by the MI of the strong toroidal magnetic field present, towards the center of the jet. At the non-linear stage both MI and kKHI are saturated, and they subsequently become weakened and quasi-steady strips of E_x are generated (see Fig. 13 below) with a kKHI modulation along the jet propagation³.

3.2 Electromagnetic fields and particle acceleration

Figure 7 shows the pattern of the electron and ion acceleration and deceleration in comparison with the structure of the electromagnetic field at $t = 900 \omega_{pe}^{-1}$ for the $e^- - i^+$ jet. The top panel (Fig. 7a) shows the $x - \gamma v_x$ distribution of the jet electrons (red), jet ions (green) and the ambient electrons (blue) electrons whilst the middle panel shows the $x - \gamma v_z$ distribution of the jet electrons (Fig. 7b). The jet ions are propagated out of phase with jet electrons as electron-positron jet as shown in 8a, however, jet ions are not accelerated as jet positrons are, due to their heavier mass. The initial $\gamma v_x = 15$ and $\gamma v_z = 0$ are marked with horizontal dashed black lines in Figures 7a and 7b,

respectively. The cross section at $x/\Delta = 540$ and it is marked with vertical dashed lines. In panel a) we see how electrons are accelerated-up in bunches between $x/\Delta \approx 550 - 900$, reaching $\gamma v_x \approx 35$. Ambient electrons are also accelerated but slightly delayed (shifted), and consequently accelerated to $\gamma v_x \approx 20$. Figure 7b showing the $x - \gamma v_z$ distribution for the jet electrons, indicates as well bunches of jet electrons accelerating mainly between $x/\Delta \approx 550 - 900$, reaching values of ≈ 10 .

Figure 7c shows the E_x component of the electric field at the cross section at the center of the jet ($z/\Delta = 381$), the strong positive electric field is located at $x/\Delta = 540$ indicated by the blue dashed line. Figure 7d shows the E_x component of the electric field in the $y - z$ plane at $x/\Delta = 540$, which is marked by the vertical lines in panels (a), (b) and (c). Black arrows indicate $B_{y,z}$. A strong electric field region visible in Fig. 7d is located near the center of the jet ($x/\Delta = 540$), which is confirmed with the collimation of jet electrons in Fig. 3d, and it corresponds to the MI mode that is dominant at this same x -location of the jet in Fig. 6d. The concentric pattern around the jet center ($m = 0$) is excited. Outside this mode, another MI is excited with $m = 5$.

Figure 8a shows the $x - \gamma v_x$ distribution of the jet (red) and the ambient (blue) electrons for the e^\pm jet in the linear stage at time $t = 600 \omega_{pe}^{-1}$. It illustrates the electron acceleration and deceleration along the jet, with some jet electrons reaching $\gamma v_x \approx 30$ at $x = 560\Delta$.

³ Supplementary movies MovieBy_eiJet.mp4, MovieBy_pairJet.mp4 at doi: [10.5281/zenodo.7017747](https://doi.org/10.5281/zenodo.7017747)

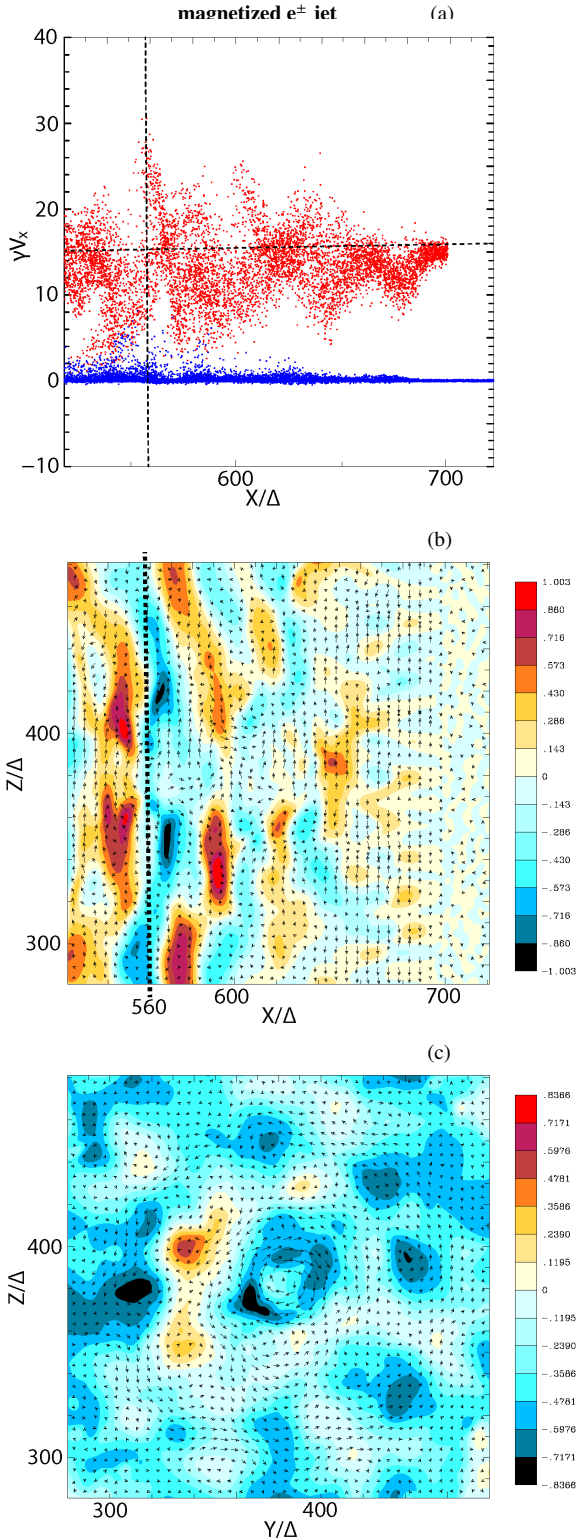


Figure 8. a) $x - \gamma v_x$ distribution of jet (red) and ambient (blue) electrons at $t = 600 \omega_{pe}^{-1}$, for an e^\pm jet. The initial $\gamma v_x = 15$ is marked with the horizontal dashed black line. b) Color map of E_x with arrows showing $B_{x,z}$ at $y/\Delta = 381$. The cross section at $x/\Delta = 560$ is marked by vertical dashed lines. c) Color map of E_x in the $y - z$ plane at $x/\Delta = 560$, marked by the vertical line in panels a and b, with arrows indicating $B_{y,z}$. The maxima and minima of E_x is (b) ± 1.003 and (c) ± 0.8366 .

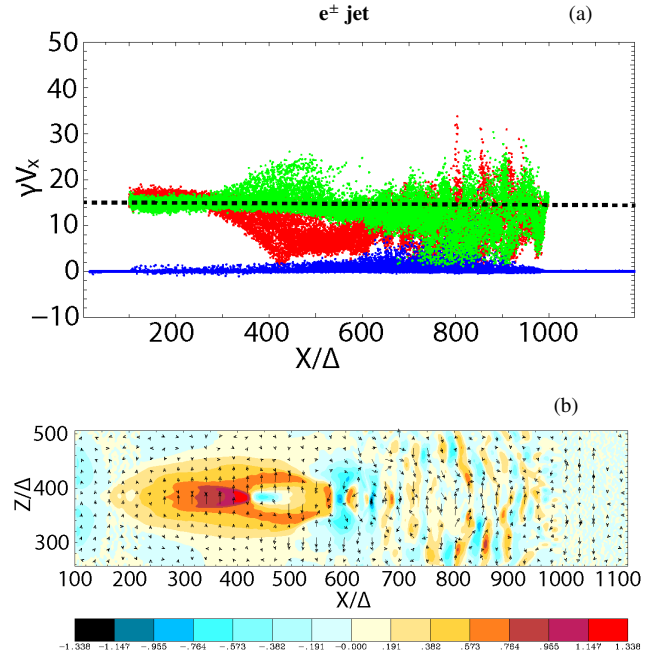


Figure 9. a) The $x - \gamma v_x$ distribution of jet electrons (red), jet positrons (green) and ambient electrons (blue) at $t = 900 \omega_{pe}^{-1}$. b) Color map of E_x in the $x - z$ plane at $y/\Delta = 381$, with arrows indicating $B_{x,z}$. The dislocation of jet electrons and positrons generates the strips of the positive and negative E_x . The maximum and minimum are ± 1.338 .

To understand how the jet electrons are accelerated we will examine the E_x in the $x - z$ (Fig. 8b) and $y - z$ (Fig. 8c) planes. The cross section is $x/\Delta = 560$ and it is marked with the vertical dashed line for comparison needs. Figures 8b and 8c show two MI modes in the transverse plane that form a symmetric, concentric pattern ($m > 5$) around the jet center ($z/\Delta = 381$) and have a wavy, complicated structure along the z direction. The jet electrons that are accelerated most significantly up to $\gamma v_x \approx 30$ are located around $x/\Delta \approx 560$ where a negative quasi-steady E_x is found at the outer layer of the jet. It is further discerned that excited MI and kKHI accelerate electrons (at the linear stage) at $x/\Delta = 560$. The kKHI modulates the jet structure along the jet propagation direction which leads to the complex electromagnetic field pattern along the jet (see also Fig. 9b). This is responsible for the stratified jet electrons (positrons), with the out-of-phase mode as will be shown in Fig. 9a below. Note that the energetic jet electrons around $x/\Delta \approx 560$ at $t = 600 \omega_{pe}^{-1}$ are accelerated further around $x/\Delta \approx 960$ at $t = 900 \omega_{pe}^{-1}$, as shown in Figs. 9a and 10c below. This indicates that the quasi-steady negative electric field propagates with the jet and accelerates the jet electrons up to $\gamma v_x \sim 35$ as shown above.

Figure 9a shows the $x - \gamma v_x$ distribution of jet electrons (red) with the out-of-phase jet positrons (green) and ambient electrons (blue), for a pair jet at $t = 900 \omega_{pe}^{-1}$. The temporal analysis of phase-velocity distributions ($x - \gamma v_x$) reveals that the bunched jet electrons (positrons) propagate with the jet velocity, which indicates that the generated patterns of E_x are quasi-steady in time as shown in Fig. 9b. To note that it is the dislocation of jet electrons and positrons which generates the strips of the positive and negative E_x . Such structures of E_x are in other words formed because the combined modes of MI and kKHI first propagate obliquely at the linear stage as shown in Figs. 8b and 8c, and later in the non-linear stage they become more vertical ($550 < x/\Delta < 900$), see Fig. 9b.

It should be noted that Figure 4c shows a rather weak B_y ($650 <$

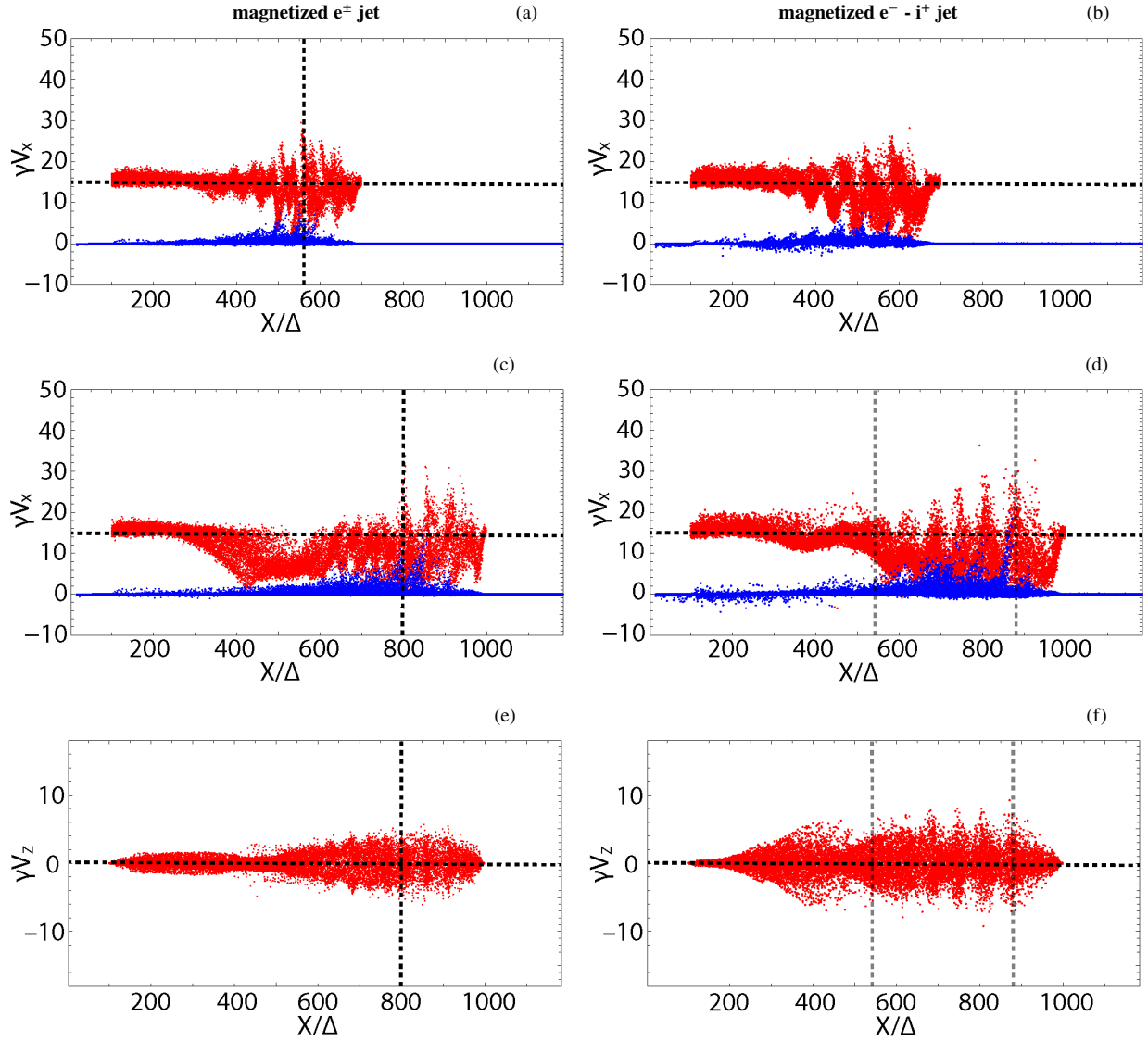


Figure 10. Phase-space $x - \gamma v_x$ distributions, for the e^\pm (a, c) jet and $e^- - i^+$ (b, d) jet, respectively, for $t = 600 \omega_{pe}^{-1}$ (upper row) and $t = 900 \omega_{pe}^{-1}$ (middle row). Panels (e) and (f) show the phase-space $x - \gamma v_z$ distributions, for the e^\pm jet and $e^- - i^+$ jet, respectively, at $t = 900 \omega_{pe}^{-1}$. In the e^\pm jet the jet electrons are slightly decelerated and later develop oscillations caused by kKHI and MI. In the $e^- - i^+$ jet, the jet electrons decelerate in bulk before the oscillatory pattern is established. The red colour indicates jet electrons, the blue colour, ambient electrons.

$x/\Delta < 1000$); however Figure 9b shows striped patterns of E_x in the $x - z$ plane at $y/\Delta = 381$, which are generated by the out-of-phase distributions of jet electrons and positrons as shown in Fig. 9a. We understand that the slight dislocations of the jet electrons and positrons constitute a response to the magnetic field structures, as the corresponding variations in v_z suggest (cf. Fig. 10e below), generating the strips of the positive and negative E_x through $\vec{E} \propto \vec{j}$. The strips of the positive and negative E_x seen in the color-map of the same figure. *In other words this means that the quasi-steady E_x accelerates jet electrons and positrons out of phase.*

Figure 10 shows the phase-space $x - \gamma v_x$ distributions for the e^\pm (a, c) jet and $e^- - i^+$ (b, d) jet respectively, for $t = 600 \omega_{pe}^{-1}$ (upper row) and $t = 900 \omega_{pe}^{-1}$ (middle row). Red colour indicates the jet electrons and blue the ambient electrons. At first glance, the phase-space distributions indicate electron acceleration at different locations. Initially the jet electrons have a Lorentz factor of $\gamma \approx 15$. Figure 10a shows that these get accelerated and decelerated by the

excited instabilities as shown in Fig. 8. Very similar behavior we see for the magnetized $e^- - i^+$ jet as well (Fig. 10a).

In figure 10c (e^\pm jet) we can observe two different stages of acceleration at $t = 900 \omega_{pe}^{-1}$: The linear stage at $300 < x/\Delta < 800$ where jet electrons are weakly accelerated and decelerated (by the MI and kKHI), and the non-linear stage at $800 < x/\Delta < 1000$, where they are considerably accelerated on three bunches. At the non-linear stage electrons reach maximum energies of $\gamma \approx 35$.

Respectively, in figure 10d for the $e^- - i^+$ jet, we can discern that the most significant acceleration occurs between $550 < x/\Delta < 900$ (linear and non-linear stage) where as we discussed above, a quasi-steady E_x prominently appears, and the jet electrons reach values of $\gamma \approx 35$. So in this case the acceleration is stronger because of the instabilities present but also because of the E_x presence (as shown in Fig. 7). Interestingly, the maximum electron energy is similar for both jet species. Also, the ambient electrons (blue) in the both jets are accelerated up to $\gamma \approx 15$ within multiple bunches, in the range

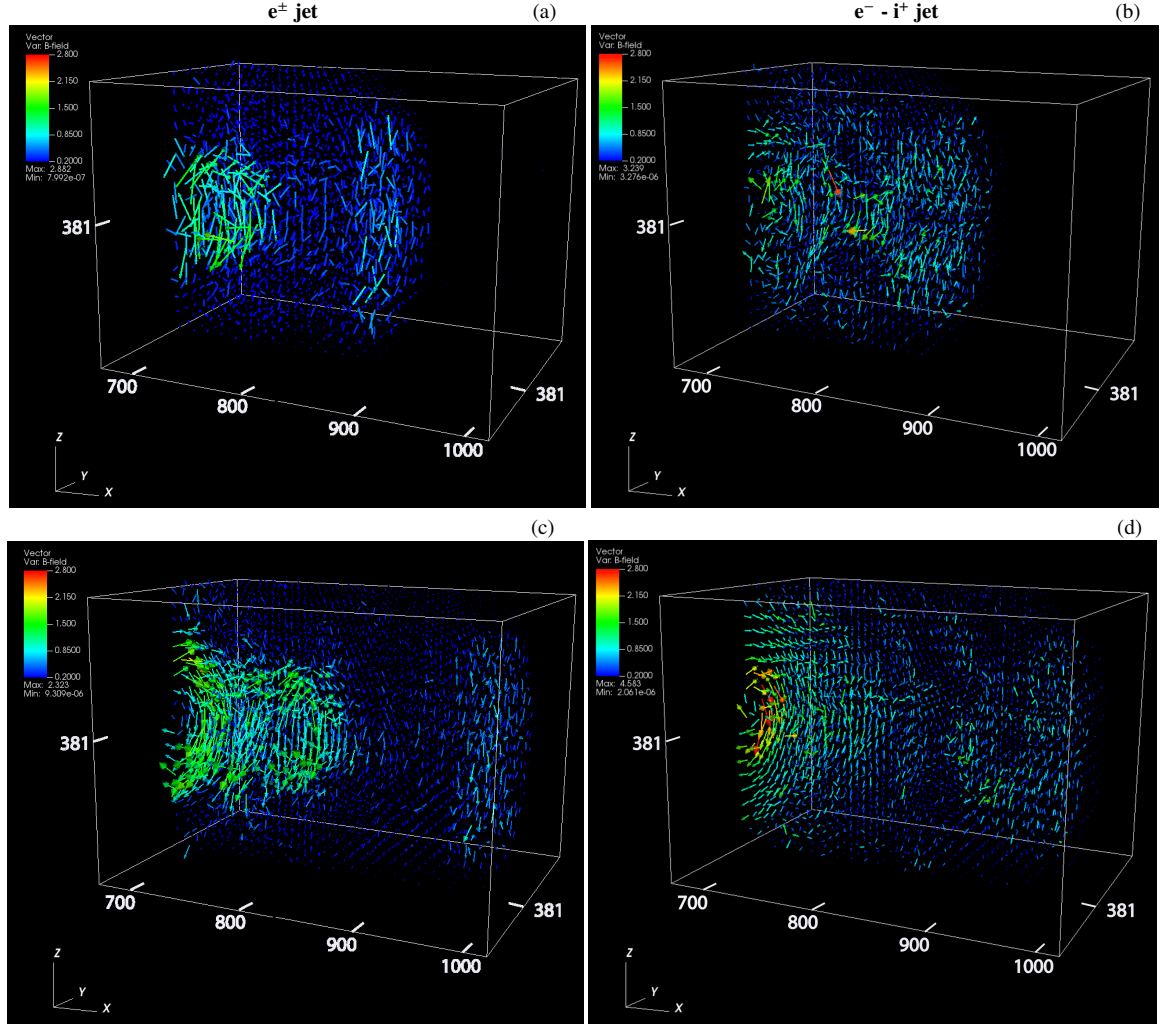


Figure 11. The magnetic field vectors within the cuboid ($670 < x/\Delta < 1020$; $256 < y/\Delta, z/\Delta < 506$) at $t = 800 \omega_{pe}^{-1}$ (first row) and $t = 900 \omega_{pe}^{-1}$ (second row) for e^\pm (panel a, c) and $e^- - i^+$ (panel b, d). The center of the jet is at $y/\Delta = z/\Delta = 381$. For the magnetic field inside the jet, the plots show half of the regions clipped at the center of jet in the $x - z$ plane ($381 < y/\Delta < 506$). The red dashed squares in Fig. 4c and 4d show the volume of these plots. The maximum and minimum of the legend of the magnetic field strength are 2.8 and 0.2.

$650 \lesssim x/\Delta \lesssim 850$, but in the $e^- - i^+$ jet ambient electrons are participating earlier in the acceleration comparing to the e^\pm jet case. There are correlations of the energy gains and losses between the ambient and the jet electrons, because the jet electrons propagate with the saturated instabilities and the peaks of the accelerated jet electrons are rather sharp. However, the ambient electrons do not move with the excited waves, and thus instead the peaks of the accelerated ambient electrons are mostly slanted toward the jet propagation. It should be noted that the acceleration of the ambient electrons stops at approximately $x/\Delta \approx 950$, which is explained by the fact that the electromagnetic fields dissipate around $x/\Delta \approx 900$.

At $t = 900 \omega_{pe}^{-1}$ the acceleration region of the ambient electrons around the e^\pm jet (Fig. 10c) approximately coincides with the jet region at $800 < x/\Delta < 950$, in which a strong magnetic turbulence after the dissipation is observed, see Fig. 11. The non-linear saturation of the instabilities ends, hence the magnetic fields dissipate and acceleration of jet electrons (not the ambient electrons) occurs.

Figures 10e and 10f, show the $x - \gamma v_z$ as a function of x/Δ for the jet electrons in e^\pm and $e^- - i^+$ jets. In the e^\pm jet, the jet electrons are strongly pinched around $400 < x/\Delta < 500$ being decelerated, while gradually start to accelerate at the later stages as stratifications

develop, caused by the kKHI and MI as shown in Fig. 10e. In contrast, Fig. 10f shows that in the $e^- - i^+$ jet, electrons are accelerated perpendicularly and some of them are reflected (in the case with $m_p/m_e = 1836$) - this is due to the large mass ratio and the slim jet used in this case - and then decelerated along the x -direction due to the MI (or kKHI) (Fig. 10d), which clearly indicates magnetic deflection, as also shown in Fig. 7 and discussed above (Figs. 7, 8). Some of the ambient electrons are also strongly accelerated as they are swept up into the relativistic jet plasma.

3.3 Three-dimensional magnetic field evolution - reconnection

Figure 11 shows the 3D evolution of the magnetic field near the jet head in the region indicated by the red rectangle in Fig. 6. The figure shows the magnetic-field vectors within a cuboid ($670 < x/\Delta < 1020$; $256 < y/\Delta, z/\Delta < 506$) at $t = 800 \omega_{pe}^{-1}$ and $t = 900 \omega_{pe}^{-1}$ for the e^\pm (a, c) and the $e^- - i^+$ (b, d) jets with their center at $y/\Delta = z/\Delta = 381$. The plots show a half-section of the jet's center in the $x - z$ plane with $381 < y/\Delta < 506$ in order to view the interior of the jets. For the e^\pm jet, the jet-head is located at $x/\Delta = 900$ at

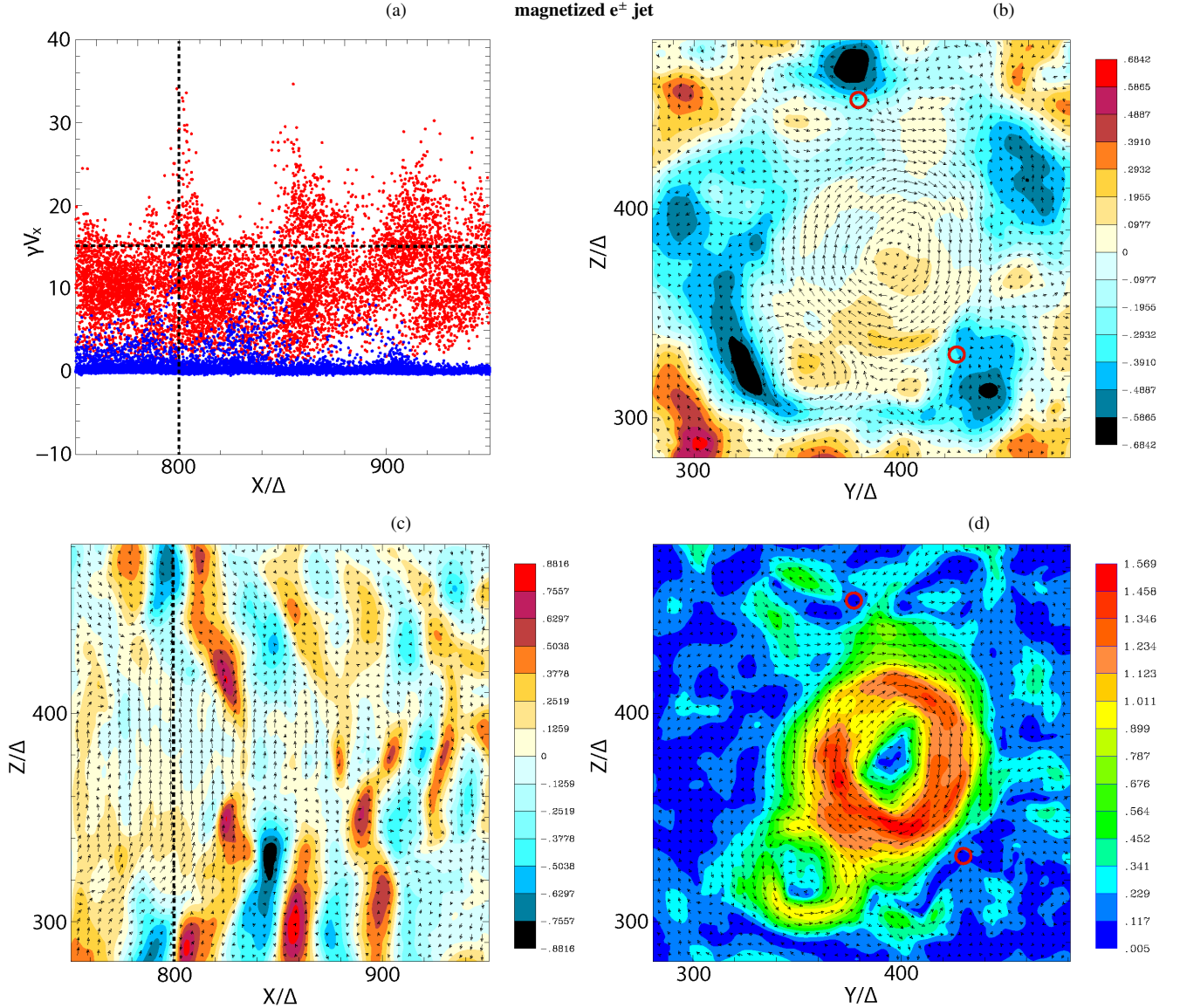


Figure 12. Possible acceleration mechanism of jet electrons in the e^\pm jet at time $t = 900 \omega_{pe}^{-1}$. a) The phase space $x - \gamma V_x$, the peak of the jet electrons (red dots) is located at $x = 800\Delta$. b) Color map of E_x in the $y - z$ plane at $x/\Delta = 800$, marked by the vertical line in panels a and c with the arrows of $B_{y,z}$. c) Color map of E_x in the $x - z$ plane at $y/\Delta = 381$, with arrows indicating (B_x, B_z) . d) the total magnetic field strength at $x/\Delta = 800$, for $281 < y/\Delta, z/\Delta < 481$. The arrows indicate the magnetic field (B_y, B_z) ; red circles indicate possible reconnection sites. The maximum and minimum values of E_x are (b): ± 0.6842 and (c): ± 0.08816 . The maximum and minimum values in panel (d) are 1.569 and 0.005, respectively.

time $t = 800 \omega_{pe}^{-1}$ (panel a), and it moves to $x/\Delta = 1000$ later at $t = 900 \omega_{pe}^{-1}$ (c). Comparing panels a) and c) one observes that the magnetic fields between $800 < x/\Delta < 1000$ first get twisted and then dissipate. Around $x/\Delta \approx 850$, at both time-steps - at the end of the linear jet evolution stage - the magnetic fields (generated by the outer MI mode) have dissipated. The magnetic fields in the inner MI mode get weak, but reappear after $x/\Delta \approx 980$, as shown in Fig. 11c. Fig. 11 indicates that a similar form of electron acceleration occurs during the dissipation of magnetic fields around $x/\Delta = 800$ for the e^\pm jet species. It is important to note that the acceleration of the electrons in the non linear stage, between $800 < x/\Delta < 1000$ is not only due to the electric field of the generated instabilities, but also it is correlated to the dissipation of the magnetic fields. At the non-linear stage the magnetic field generated by instabilities dissipates, and although the

cause of this is not clear presently, it might be due to the termination of the non-linear saturation as described by Blandford et al. (2017).

The $e^- - i^+$ jet, in Figure 11b, shows a weakened magnetic field at the jet centre, surrounded by swirling magnetic fields. For this jet the front edge of the toroidal magnetic field at the centre is peeled-off during the jet propagation, as seen in Fig. 11d. This indicates that the toroidal magnetic field might have dissipated at the non-linear stage and as a consequence moved towards the jet boundary where flux ropes are formed, as discussed in Blandford et al. (2017), see Figs. 12 and 13.

Figure 12 shows four different plots indicating a possible acceleration mechanism of jet electrons for an e^\pm jet, at $t = 900 \omega_{pe}^{-1}$. Figure 12a shows the phase space $x - \gamma V_x$. The peak of the jet electrons (red dots) is located at $x = 800\Delta$. A color map of E_x is shown in Fig. 12b with the arrows of $B_{y,z}$ marked by the vertical line in Fig. 12a, at

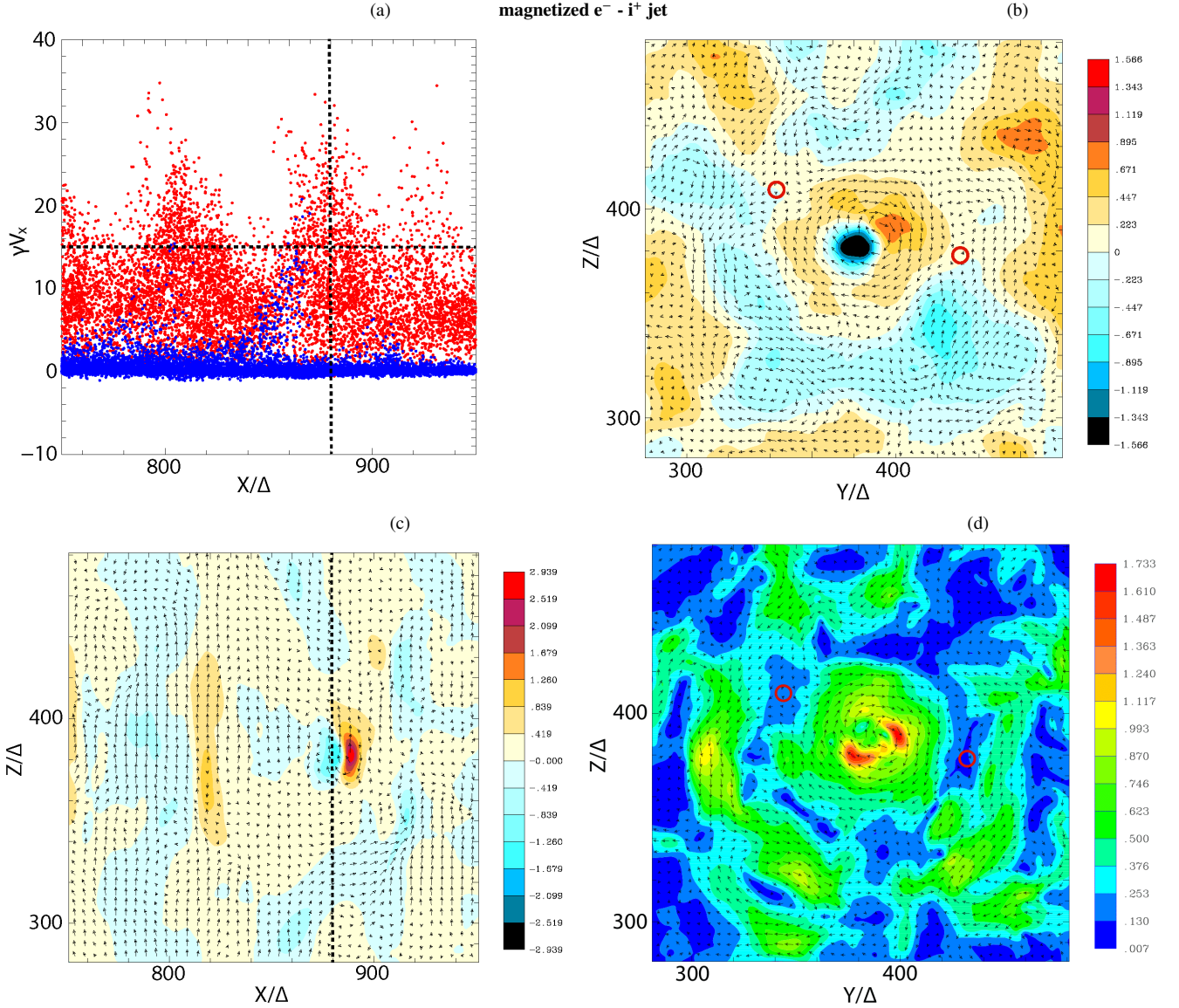


Figure 13. Possible acceleration mechanism of jet electrons in the $e^- - i^+$ jet at time $t = 900 \omega_{pe}^{-1}$. a) The phase space $x - \gamma V_x$, the peak of the jet electrons (red dots) is located at $x = 880\Delta$. b) Color map of E_x in the $y - z$ plane at $x/\Delta = 880$ marked by the vertical line in panel a with the arrows of $B_{y,z}$. c) Color map of E_x in the $x - z$ plane at $y/\Delta = 381$, with arrows indicating (B_x, B_z) . d) the total magnetic field strength at $x/\Delta = 880$, for $281 < y/\Delta, z/\Delta < 481$. The arrows indicate the magnetic field (B_y, B_z) ; red circles indicate possible reconnection sites.

$x/\Delta = 800$. The strong negative E_x near the jet boundary is responsible for the acceleration of electrons. Figure 12c correspondingly shows a colour map of E_x in the $x - z$ plane at $y/\Delta = 381$, with the arrows indicating a (B_x, B_z) . Figure 12d shows the total magnetic field strength at $x/\Delta = 800$, for $281 < y/\Delta, z/\Delta < 481$. The arrows indicate the magnetic field components (B_y, B_z) ; red circles indicate possible reconnection sites. As a necessary condition, the reconnection location should coincide with the regions of minimum magnetic field strength, indicated by the dark blue color in Fig. 12d. The red circles indicate possible reconnection sites where the magnetic fields are oriented on the opposite direction.

For an $e^- - i^+$ jet we correspondingly show in Fig. 13 four panels, indicating a possible acceleration mechanism for the jet electrons, at time $t = 900 \omega_{pe}^{-1}$ comparable to Fig. 12. Panel a) shows the phase space $x - \gamma V_x$ where the peak of the jet electrons (red dots) is located at $x = 880\Delta$. A color map of the electric field component E_x with

the arrows of the magnetic field component $B_{y,z}$ is shown in panel b). The strong negative E_x at the center of the jet is responsible for the electron acceleration. Panel c) depicts a color map of E_x in the $y - z$ plane at $x/\Delta = 880$, marked by the vertical line in panel a), with arrows indicating the (B_y, B_z) . Panel d) shows the total magnetic field strength at $x/\Delta = 880$, for $281 < y/\Delta, z/\Delta < 481$. The arrows indicate the magnetic field (B_y, B_z) and the red circles on panels b and d, indicate possible reconnection sites.

What we observe in this study is that the inner MI mode becomes dominant due to the collimation of the jet electrons, which generate the clockwise circular magnetic field. At the same time, the outer MI mode in the jet starts to split, resulting in a number of magnetic structures through the residues of the MIs. These structures are found in the areas of weak magnetic fields (blue) where swirling and/or oppositely directing magnetic fields exist, thus a possible reconnection site is marked by a red circle where the direction of the magnetic

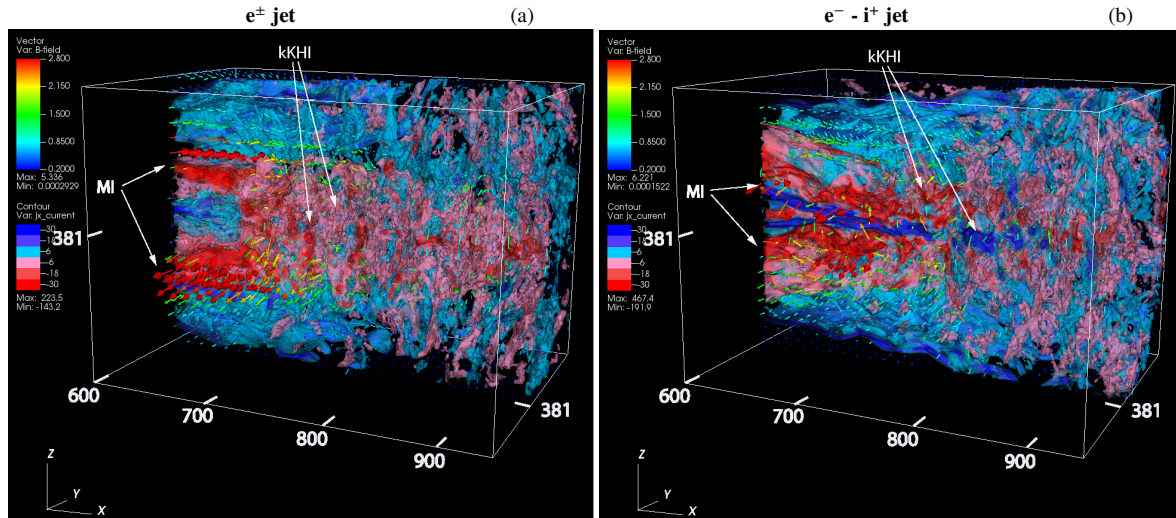


Figure 14. The x -component J_x of the current within a cuboid of $600 < x/\Delta < 950$; $256 < y/\Delta, z/\Delta < 506$ at $t = 1000 \omega_{pe}^{-1}$ for an e^\pm (a) and $e^- - i^+$ (b) jet. Both plots show the cross section at the centre of the jet ($y/\Delta = z/\Delta = 381$). The blue dashed squares in Fig. 4c and 4d show the volume of these plots. There is an overlap with Figs. 11c and 11d including the range $770 < x/\Delta < 1120$.

fields changes. In Fig. 12d specifically, we see typical morphologies of a magnetic reconnection site. In our simulation results we have observed that possible reconnection sites are surrounded by oppositely swirling magnetic field patterns with a minimum magnetic field strength (dark blue). Note that the magnetic fields are produced by the jet current modulated by the excited kKHI and MI. At this time the outer MI mode is dissipated as shown in Fig. 11c as well where the magnetic field is weak near the jet boundary. The toroidal field structure gets distorted and dispersed, as also seen in the movies⁴ provided as supplementary material for the two jet compositions (electron-positron and electron-ion), showing the spatial evolution of the magnetic field and their differences. Subsequently comparing panels d) of Figs. 12, 13 while inspecting the provided movies, one discerns how the magnetic field gets reorganized and forms multiple magnetic flux ropes. The supplemental movies for both magnetized jet compositions⁵ further show that the magnetic structures interact with each other and with the surrounding environment, generating the right conditions for magnetic reconnection.

3.4 Non-linear instabilities growth and acceleration

To investigate the transition from the late linear stage to the non-linear stage, Figure 14 shows the 3D magnetic field vectors within a cuboid of $600 < x/\Delta < 950$, $256 < y/\Delta, z/\Delta < 506$ (indicated by the red dashed square in Fig. 4c and 4d) at $t = 1000 \omega_{pe}^{-1}$ for e^\pm and $e^- - i^+$ jets. For the magnetic field to be shown inside the jet, the plots depict half of the jet regions clipped at the center of jet in the $x - z$ plane ($381 < y/\Delta < 506$). Note that these plots overlap with Fig. 11 at $x/\Delta = 770$. Beyond $x/\Delta = 750$ for the e^\pm jet, a magnetic field disruption of the outer mode of the MI occurs, resulting in a disordering via a non-linear saturation of the kKHI & MI, that is seen up to $x/\Delta \approx 950$. Around $x/\Delta = 780$ as the magnetic field near the

jet boundary dissipates, the magnetic field near the centre of the jet gets dissipated around $x/\Delta = 820$.

Figure 14a shows the growth of the kKHI and MI (and of the WI) as well as the generation of two modes of MIs (indicated by the two red dotted lines in Fig. 6c), along the jet radius (z) up to $x/\Delta = 750$. These correspond to the groups of accelerated and decelerated bunches of electrons in the calculated phase-space distributions shown in, e.g., Fig. 10c.

Note that without the magnetic field the jets propagate collimated, but instabilities push the jet particles out of the original jet boundary, as shown in Figs. 2a,b, in particular at the non-linear stage. Moreover, in Figs. 4c,d all jets are collimated most probably due to the MI. On the other hand with a toroidal magnetic field the MI grows stronger, therefore the jet electrons are stronger collimated.

At around $x/\Delta = 700$ the collimated jet structure becomes weakened and stratified, as shown in Fig. 14a. This indicates the existence of a late non-linear stage of the MI and kKHI. The MI mode near the jet boundary dissipates around $x/\Delta = 750$ first, but the inner mode (MI and kKHI) stays longer and dissipates at approximately $x/\Delta = 800$, which are more easily recognized in Figs. 11a,c. It is important to note that by comparing the previous panels of Fig. 11 with Figs. 6 and 12, the 3D perspectives indicate distinctive differences in the location of the magnetic flux ropes and vector directions, contrary to the information extracted from the 2D projections onto the $y - z$ and $x - z$ planes. The latter indicates that the viewing-angle sensitivity should be taken into account for future studies combined with observational jet polarization maps, as we will discuss in the following section. In a future work we will use larger set-ups to investigate comparable cases with observed astronomical sources. Figure 14b shows the strong negative current in the center of the jet and the toroidal magnetic field which is opposite to the original direction.

Figure 15 shows the energy distribution of the jet (red) and ambient (blue) electrons in and around the e^\pm and $e^- - i^+$ jet in the two regions $x/\Delta < 550$ and $x/\Delta > 550$ at $t = 900 \omega_{pe}^{-1}$. We see that the electron acceleration is mostly significant in the non-linear stage ($x/\Delta > 550$). We observe significant acceleration for both cases reaching Lorentz factors of $\gamma \sim 35 - 40$. Specifically, for the magnetized $e^- - i^+$ jet, the jet electrons even in the non-linear stage are more efficiently accelerated compared to the non-linear stage of the e^\pm jet case,

⁴ The total magnetic field in the $y - z$ plane at $289 < y/\Delta, z/\Delta < 480$; for e^\pm and $e^- - i^+$ jets respectively, see supplementary videos MovieBtot_pairJet.mp4, MovieBtot_eiJet.mp4, at doi:10.5281/zenodo.7017747

⁵ see MovieBtot_pairJet.mp4, MovieBtot_eiJet.mp4 at doi: 10.5281/zenodo.7017747

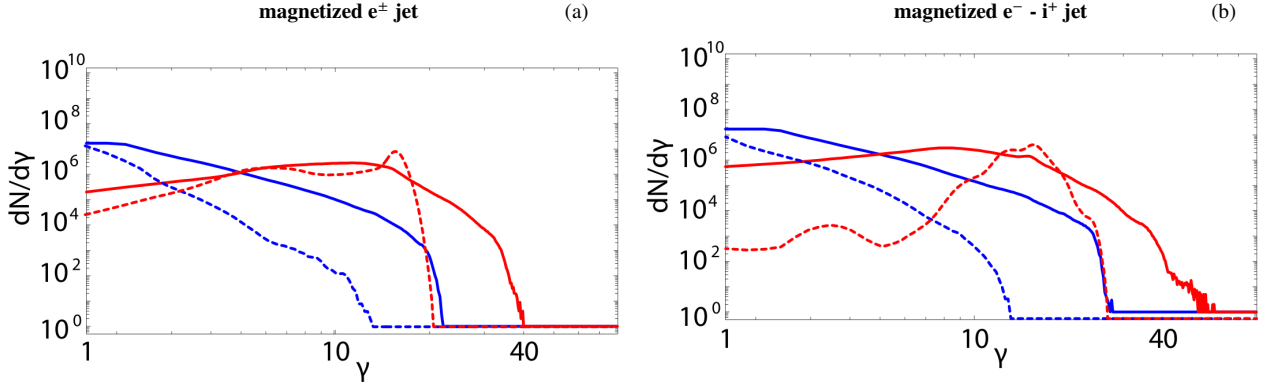


Figure 15. Particle energy distributions of the jet (red) and ambient (blue) electrons in and around the e^\pm jet (a) and $e^- - i^+$ jet (b) in the two regions $x/\Delta < 550$ (dashed lines) and $x/\Delta > 550$ (solid lines) at $t = 900 \omega_{pe}^{-1}$.

reaching a maximum of Lorentz factor ~ 45 . Nevertheless for the e^\pm jet, the jet electrons are mostly accelerated in the non-linear stage reaching a maximum Lorentz factor of 40.

Comparing Figs. 15 and 10 we deduce that the jet electrons are further accelerated once a dissipation of the magnetic fields occurs in the non-linear stage, as it is also similarly seen in the kinetic simulations of driven magnetized turbulence (e.g., Zhdankin et al. 2018). Note that in the latter simulation studies, the turbulent magnetic fluctuations were externally forced into the simulation system and therefore were not self-consistent. On the contrary, the turbulent magnetic field in our simulations (where we see multiple magnetic flux ropes (e.g. in Figs. 6-11)) is self-consistently created in the relativistic jets, through the self-consistent dissipation of the toroidal magnetic field. Previous studies (Kowal et al. 2011, 2012; Lazarian et al. 2016) discuss the particle acceleration process in turbulent magnetic reconnection. Comisso & Sironi (2018) have investigated particle acceleration at reconnecting current sheets due to stochastic interactions with turbulent fluctuations (plasmoids and vertexes). In our simulations at the non-linear stage, it is comprehensible to claim that plasmoids (vertexes) are generated as shown above which may accelerate jet electrons in a similar way.

4 SUMMARY AND DISCUSSION

We have conducted extensive 3D PIC simulations to study the spatio-temporal evolution of magnetized relativistic electron-positron and electron-ion (electron-proton) jets, examining their kinetic instabilities and the associated particle acceleration. We investigated the excited kinetic instabilities and the associated magnetic fields at the linear and non-linear stage, as they may occur in astrophysical relativistic jets. The dissipation of the magnetic fields was observed to generate electric fields that are sufficiently strong to further accelerate particles to Lorentz factors of up to around 35.

In this work we used a new jet injection scheme. We injected both e^\pm and $e^- - i^+$ jets, with a co-moving toroidal magnetic field while we used a top-hat jet density profile. The current was self-consistently carried by the jet particles, $\mathbf{J} = \nabla \times \mathbf{B}$. In order to sustain the toroidal magnetic field carried by the jet, the current was applied at the jet orifice and a motional electric field was applied in order to compensate the bending by the applied toroidal magnetic field. Both jets were initially moderately magnetized while the ambient medium remained unmagnetized. In the new jet injection scheme we applied the induced electric field $E_x = \nabla B_\phi$ in order to avoid a non-linear

growth. We have run the simulations sufficiently long in order to examine the non-linear effects of the jet evolution.

We found that the dominant excited modes of instabilities depend on the different jet compositions. Three different instabilities (WI, MI, kKHI) grow in similar timescales, however, depending on the plasma conditions (unmagnetized, different species) some instabilities grow faster and stronger. Particularly the MI grows faster and stronger with larger mass ratio (4 and 1826) and an excitation of the MI or kKHI is weaker for the unmagnetized case. In general, stronger MI and kKHI grow in the jets with toroidal magnetic fields. The MI and kKHI are associated with a quasi-steady electric field (E_x) for both jet species. These accompanied electric fields accelerate and decelerate electrons and positrons. Additionally we found that the electrons can be further accelerated by the development of twisted and turbulent magnetic fields which are generated by the dissipation of the toroidal magnetic fields possibly accompanying reconnection. For an e^\pm jet, the MI is excited combined with a kKHI, while the produced quasi-steady E_x modulates the jet particles. For the electron-ion jet, the jet electrons are pinched dominantly by the MI at the later linear stage. Further simulations will be important to decisively confirm possible supplemental acceleration mechanisms with varying simulation parameters such as, jet radius, magnetization factor, jet density profile, etc. From the present extensive simulation studies we conclude, that a moderate initial magnetic field can change the development of the kinetic plasma instabilities, for different jet species, even if the instabilities significantly amplify the magnetic field, here by factors reaching 50.

Figure 8 shows that the quasi-steady electric fields accelerate and decelerate jet electrons at the linear stage and that the consequent magnetic field dissipation accelerates jet electrons further at the non-linear stage (Fig. 12) for the e^\pm jet. At the non-linear stage we also observed that jet electrons propagate outside the jet and that the jet boundaries seem to get distorted by the kKHI. Near the jet head of the e^\pm jet we witness a re-arrangement of the magnetic field and a general weakening of the currents with some vortices (shown in Fig. 12d). We found that at the initial stages along the jet a strong toroidal magnetic field is maintained by a strong $-J_x$ current associated with collimated jet (ambient) electrons.

The magnetic field generated and amplified by different instabilities, in the non-linear stage dissipates and reorganizes into a new topology. The 3D magnetic field topology (Fig. 11) indicates possible reconnection sites and the electrons accelerated in the linear stage are significantly re-accelerated in the non-linear stage up to a Lorentz factor of 35, accompanied by the dissipation of the mag-

netic field possibly associated with the reconnection, which requires further investigation.

We have identified potential sites of magnetic reconnection in our simulations; however, an unambiguous determination in 3D is not trivial. The magnetic field structure of a reconnection site in 2D simulations consists of X and O shapes which can be recognized rather easily by the changes of the magnetic field direction and the position of null (very weak) magnetic fields in the 2D projections. The complex structures of 3D reconnections have been investigated in e.g., Parnell et al. (2010); Lalescu et al. (2015); Lazarian et al. (2016); Bentkamp et al. (2019); Lazarian et al. (2020); Borissov et al. (2020). In order to determine the reconnection locations analytically, we would need to investigate the eigenvalues of Jacobian matrix, which is beyond the scope of this work, for more details, see Cai et al. (2007).

It is evident that the currents and magnetic structures are very different for $e^- - i^+$ and e^\pm jets. These differences arise from the different mobilities of ions and positrons manifested in the polarization signatures of radiation. It follows that the resulting magnetic field structures are different enough to yield distinctive polarizations in VLBI (Very Long Baseline Interferometry) observations of AGN jets at the highest angular resolutions (e.g., Gomez et al. 2016). For example, toroidal magnetic fields (like in our simulations) inside and outside of an $e^- - i^+$ jet contribute to circular polarization. This may help us to distinguish an $e^- - i^+$ jet clearly from an e^\pm jet, at least partially, and in accordance with the present and recent studies, also to establish if and when a possible dissipation of the swirling magnetic fields occur in accordance with the present and recent studies (e.g. Nishikawa et al. 2020).

The present work is an important first step from a future follow-up simulation studies with larger jet radii that will cover more modes of kinetic instabilities. Therefore, although our present results offer important insights, we expect that larger simulations will shed further light onto understanding the evolution of different jet species, the dissipation of twisted magnetic fields, the consequent development of electric and magnetic field instabilities, organized magnetic patterns, reconnection events, and particle acceleration which are critical to observational astronomy.

VLBI observations of AGN jets are not sufficient to distinguish signatures of different jet plasma compositions. Circular polarization (CP) has been detected so far in a limited number of AGN jets (e.g., Wardle et al. 1998; Homan & Wardle 1999; Homan et al. 2001; Gabuzda et al. 2008; Thum et al. 2018), in all cases at very low percentage levels that do not exceed $1 - 2\%$, in contrast to the relatively high values of linear polarization that usually can reach $30 - 40\%$. CP in AGN jets can be produced either as an intrinsic component of the synchrotron radiation (for electron-ion jets), or through Faraday conversion of linear polarization (Jones & O'Dell 1977), the latter appearing to be the prevailing mechanism (e.g., Wardle et al. 1998; Gabuzda et al. 2008). Constraints on the jet composition requires not only extremely accurate CP measurements, but also a robust determination of the three-dimensional magnetic field structure, in order to quantify the level of Faraday conversion from linear to circular polarization (Wardle & Homan 2003), as well as stringent constraints on the energy distribution of radiating particles, see Wardle et al. (1998).

There are currently a lot of efforts, both within the MOJAVE and BU Blazar programs (e.g., Jorstad et al. 2005; Pushkarev et al. 2012), to generate additional VLBI images of CP which will help advance our knowledge. In addition, the participation of phased ALMA in VLBI arrays, such as the Event Horizon Telescope and the GMVA (e.g., EHT Collaboration 2019; Issaoun et al. 2021; Goddi et al.

2021) provides a significant boost in sensitivity that will allow a better characterization of the CP in AGN jets, and most importantly the CP spectra which may hold the key to determine the jet composition.

We propose that several of the complicated magnetic field structures we report in this work could be observed and verified in the near future with polarimetric VLBI observations at extremely high angular resolutions, if they can resolve the transverse structure of the jet, as with space VLBI (e.g., Gomez et al. 2016; Giovannini et al. 2018) and with the Event Horizon Telescope (e.g., EHT Collaboration 2019; Kim et al. 2020). For example, flares may be found associated with reconnection where the dissipation of a significant fraction of the magnetic energy occurs. Particularly, this may happen when an accelerated particle beam is directed along the line of sight (see Komissarov 2012; McKinney & Uzdensky 2012; Sironi et al. 2015). Our study might have important implications in this context such as for example, the prompt GRB emission which could be due to reconnection events (e.g., Metzger 2027; Burns 2020; Zhang 2018). Our immediate future work aims to investigate this phenomenon by combining observations with the temporal and spectral properties of simulation studies by applying simulations with a systematic parameter survey in order to understand the jet evolution with toroidal magnetic fields and with Gaussian (not top-hat) jet density profiles.

DATA AVAILABILITY

The data underlying this article will be shared on reasonable request to the corresponding author. The supplementary videos for this publication can be obtained from [doi: 10.5281/zenodo.7017747](https://doi.org/10.5281/zenodo.7017747)

ACKNOWLEDGEMENTS

The authors would like to thank the collaborators Martin Pohl and Jacek Niemiec for the insightful discussions during the development of this work. This work was supported by the NASA-NNX12AH06G, NNX13AP-21G, and NNX13AP14G grants. Recent work was also provided by the NASA through Chandra Award Number GO7-18118X (PI: Ming Sun at UAH) issued by the Chandra X-ray Center, which is operated by the SAO for and on behalf of the NASA under contract NAS8-03060. The simulations presented in this report have been performed by Frontera supercomputer at the Texas Advanced Computing Center under the AST21038: Computational Study of Astrophysical Plasmas, and also provided by the NASA through by the grant: Nature Of Hard X-rays From A TeV-detected RadioGalaxy (PI: Ka Wah Wong at SUNY Brockport) issued by the NuSTAR Guest Observer Cycle 6 2019. Y.M. is supported by the ERC Synergy Grant “BlackHoleCam: Imaging the Event Horizon of Black Holes” (Grant No. 610058). The work of I.D. has been supported by the NUCLEU project. Simulations were performed using Pleiades and Endeavor facilities at NASA Advanced Supercomputing (NAS: s2004), using Comet at The San Diego Supercomputer Center (SDSC), and Bridges at the Pittsburgh Supercomputing Center, which are supported by the NSF. JLG acknowledges the support of the Spanish Ministerio de Economía y Competitividad (grants AYA2016-80889-P, PID2019-108995GB-C21), the Consejería de Economía, Conocimiento, Empresas y Universidad of the Junta de Andalucía (grant P18-FR-1769), the Consejo Superior de Investigaciones Científicas (grant 2019AEP112), and the State Agency for Research of the Spanish MCIU through the Center of Excellence Severo Ochoa award for the Instituto de Astrofísica de Andalucía (SEV-2017-0709).

REFERENCES

- Alves, E.P., Grismayer, T., Martins, S.F., Fiuza, F., Fonseca, R.A., & Silva, L.O., 2012, *ApJ*, 746, L14
- Alves, E.P., Grismayer, T., Fonseca, R.A., Silva, L.O., 2015, *Phys. Rev. E*, 92, 021101
- Ardaneh, K., Cai, D., Nishikawa, K.I., 2016, *ApJ*, 827, 124
- Ascenzi, S., Oganessian, G., Branchesi, M., Ciolfi, R., 2021, *Electromagnetic counterparts of compact binary mergers*, *Journal of Plasma Physics* 87, 845870102
- Bentkamp, L., Lalescu, C. C., Wilczek, M., 2019, *Nature communications*, Volume 10, id. 3550
- Blandford, R., Meier, D., Readhead, A., 2019, *ARA & A*, 57, 467
- Blandford, R., Yuan, Y., Hoshino, M., Sironi, L., 2017, *Space Sci Rev*, 207, 291
- Borisov, A., Neukirch, T., Kontar, E. P., Threlfall, J., and Parnell, C. E., 2020, *A&A*, 635, A63
- Bret, A., 2009, *ApJ*, 699, 990
- Bret, A., Dieckmann, M. E., Gremillet, L., 2010, *Ann. Geophys.*, 28, 2127
- Bret, A. and Dieckmann, M. E., 2010, *Physics of Plasmas* 17, 032109
- Bromberg, O., Nakar, E. Piran, T., and Sari, R., 2011, *ApJ*, 740, 100
- Buneman, O. 1993, in *Computer Space Plasma Physics: Simulation Techniques and Software*, Eds.: Matsumoto & Omura, Tokyo: Terra, p.67
- Burns, E., 2020, *Living Reviews in Relativity*, 23, 4
- Cai, D.S., Nishikawa, K.-I., Lembege, B., 2007, in *Advanced Methods for Space Simulations*, edited by H. Usui and Y. Omura, TERRAPUB, Tokyo, pp. 145-166
- Christie, I. M., Lalakos, A., Tchekhovskoy, A., Fernandez, R., Foucart, F., Quataert, E., Kasen, D., 2019, *MNRAS*, 490, 4811
- Comisso, L., Sironi, L., 2018, *Phys. Rev. Lett.*, 121, 255101
- Daughton, W., Roytershteyn, V., Karimabadi, H., et al. 2011, *Physics Nature*, 7, 539
- de Gouveia Dal Pino, E. M., & Lazarian, A., 2005, *A&A* 441, 845
- de Gouveia Dal Pino, E. M., Piovezan, P. P., Kadowaki, L. H. S. 2010, *A&A*, 518, 5
- de Gouveia Dal Pino, E. M., Alves Batista, R., Kowal, G., Medina-Torrejón, T., Ramirez-Rodriguez, J. C. 2018, *BHCB2018*
- Dieckmann, M.E., Shukla, P.K., Drury, L.O.C., 2008, *ApJ*, 675, 586
- Drenkhahn, G., & Spruit, H. C., 2002, *A&A* 391, 1141
- EHT Collaboration, 2019, *ApJL*, 875, L1
- Fowler, T. K., Li, H., Anantua, R., 2019, *ApJ*, 885, 4
- Gabuzda, D., 2019, *Galaxies*, 7, 5
- Gabuzda, D., et al. 2008, *MNRAS*, 384, 1003
- Giannios, D., Uzdensky, D. A., & Begelman, M. C., 2009, *MNRAS*, 395, L29
- Giannios, D., 2010, *MNRAS*, 408, L46
- Giannios, D., 2013, *MNRAS*, 431, 355
- Giovannini, G., et al. 2018, *Nature Astronomy*, 2, 472
- Goddi, C., Martí-Vidal, I., Messias, H., et al., 2021, *ApJL*, 910, L14
- Granot, J., 2012, *MNRAS*, 421, 2442
- Grismayer, T., Alves, E. P., Fonseca, R. A. and Silva, L. O., *Phys. Rev. Lett.* 2013, 111, 015005
- Gómez, José L., Lobanov, Andrei P., Bruni, Gabriele, Kovalev, Yuri Y., Marscher, Alan P., Jorstad, Svetlana G., Mizuno, Yosuke, Bach, Uwe, Sokolovsky, Kirill V., Anderson, James M., Galindo, Pablo, Kardashev, Nikolay S., Lisakov, Mikhail M., 2016, *ApJ*, 817, 96
- Guo, F., Liu, Y.-H., Daughton, W., & Li, H., 2015, *ApJ*, 806, 167
- Guo, F., Li, H., Daughton, W., et al., 2016a, *ApJL*, 818, L9
- Guo, F., Li, H., Daughton, W., Li, X., & Liu, Y.-H., 2016b, *PhPI*, 23, 0055708
- Hawley, J. F., Fendt, C., Hardcastle, M., et al., 2015, *Space Sci. Rev.*, 191, 441
- Homan, D.C. & Wardle, J.F.C., 1999, *AJ*, 118, 1942
- Homan, D.C. et al. 2001, *ApJ*, 556, 113
- Homan, D.C. et al. 2006, *AJ*, 131, 1262
- Homan, D.C. et al. 2009, *ApJ*, 696, 328
- Issaoun, S., Johnson, M. D., Blackburn, L., et al. 2021, 2021, *ApJ*, 915, 99
- Jaroschek, C.H., Lesch, H., Treumann, R.A., 2005, *ApJ*, 618, 822
- Jones & O'Dell, 1977 *A&A*, 61, 291
- Jorstad, S. G., Marscher, A. P., Lister, M. L., et al. 2005, *AJ*, 130, 1418
- Kadowaki, L. H. S., De Gouveia Dal Pino, E. M., Stone, J. M., 2018, *ApJ*, 864, 52
- Kadowaki, L. H. S., de Gouveia Dal Pino, E. M., Medina-Torrejón, T. E. PoS Kagan, D., Milosavljevic, M., & Spitkovsky, A., 2013, *ApJ*, 774, 41
- Karimabadi, H., Roytershteyn, V., Vu, H. X., et al., 2014, *PhPI*, 21, 2308
- Kato, T. N. & Takabe, H., 2010, *ApJ*, 721, 828
- Kim, J-Y, et al. 2020, *A&A*, 640, A69
- Komissarov, S. S., 2012, *MNRAS*, 422, 326
- Kowal, G., de Gouveia Dal Pino, E.M., Lazarian, A., 2011, *ApJ*, 735, 102
- Kowal, G., de Gouveia Dal Pino, E. M., Lazarian, A., 2012, *Phys. Rev. Lett.*, 108, 241102
- Lalescu, C. C., Shi, Yi-K., Eyink, G. L., Drivas, T. D., Vishniac, E. T. and Lazarian, A., 2015, *Phys. Rev. Lett.* 115, 025001
- Lazarian, A., Kowal G., Takamoto M., de Gouveia Dal Pino E.M., Cho J. 2016, *Theory and Applications of Non-relativistic and Relativistic Turbulent Reconnection*. In: Gonzalez W., Parker E. (eds) *Magnetic Reconnection. Astrophysics and Space Science Library*, vol 427. Springer, Cham. arxiv:1512.03066
- Lazarian, A., Eyink, G. L., Jafari, A., Kowal, G., Li, H., Siyao Xu, S., and Vishniac, E. T., 2020, *Phys. Plasmas*, 27, 012305
- Liang, E., Boettcher, M. and Smith, I., 2013a, *ApJL*, 766, L19
- Liang, E., Fu, W., Boettcher, M., Smith, I. and Roustazadeh, P., 2013b, *ApJL*, 779, L27
- MacDonald, N.R. & Nishikawa, K.-I., 2021, *A&A*, A10, 653
- Matsumoto, Y., Amano, T., Kato, T. N., Hoshino, M., 2017, *Phys. Rev. Lett.*, 119, 105101
- McKinney, J. C., & Uzdensky, D. A., 2012, *MNRAS*, 419, 573
- Meli, A. & Nishikawa, K., 2021, *Universe*, 7, 450
- Metzger, B. D., 2017, *Living Reviews in Relativity*, 20, 3
- Mizuno, Y., Hardee, P. E., & Nishikawa, K.-I., 2014, *ApJ*, 784, 167
- Niemiec, J., Pohl, M., Stroman, T., & Nishikawa, K.-I., 2008, *ApJ*, 684, 1174-1189
- Nishikawa, K.-I., Hardee, P., Richardson, G., Preece, R., Sol, H., Fishman, G.J., 2003, *ApJ* 595, 555
- Nishikawa, K. -I., J. Niemiec, M. Medvedev, H. Sol, P. Hardee, Y. Mizuno, B. Zhang, M. Pohl, M. Oka, D. H. Hartmann, 2009, *ApJ*, 698, L10
- Nishikawa, K.-I., Hardee, P., Zhang, B., Dutan, I., Medvedev, M., Choi, E.J., Min, K.W., Niemiec, J., Mizuno, Y., Nordlund, Å., Frederiksen, J.T., Sol, H., Pohl, M., Hartmann, D.H., 2013, *Ann Geophys* 31, 1535
- Nishikawa, K.I., Hardee, P.E., Duţan, I., Niemiec, J., Medvedev, M., Mizuno, Y., Meli, A., Sol, H., Zhang, B., Pohl, M., et al., 2014, *ApJ*, 793, 60
- Nishikawa, K.-I., Frederiksen, J. T., Nordlund, Å., et al., 2016a, *ApJ*, 820, 94
- Nishikawa, K.-I., Mizuno, Y., Niemiec, J., et al., 2016b, *Galaxies*, 4, 38
- Nishikawa, K.-I., Mizuno, Y., Gómez, J. L., et al., 2017, *Galaxies*, 5, 58
- Nishikawa, K.-I., Mizuno, Y., Gómez, J. L., et al., 2019, *Galaxies*, 7, 29
- Nishikawa, K.-I., Mizuno, Y., Gómez, J. L., et al., 2020, *MNRAS*, 493, 2652
- Nishikawa, K.-I., Dutan, I., Köhn, C., Mizuno, Y., *Living Reviews in Computational Astrophysics*, 2021, 7:1
- Oka, M., Fujimoto, T. K., Nakamura, M., et al. 2008, *Phys. Rev. Lett.*, 101, 205004
- Ruiz, M., Shapiro, S. L., Tsokaros, A., 2018, *Phys. Rev. D*, 97 (2): 021501
- O'Sullivan, S.P., McClure-Griffiths, N.M., Feain, I.J., Gaensler, B.M., Saul, R.J. 2013, *MNRAS*, 435, 311
- Parnell, C. E., Rhona C. Maclean, R. C., Haynes, A. L. and Galsgaard, K., *Astrophysical Dynamics: From Galaxies to Stars Proceedings IAU Symposium No. 271*, 227, 2010
- Pushkarev, A. B., Hovatta, T., Kovalev, Y. Y., et al., 2012, *A&A*, 545, AA113
- Rieger, F. M. & Duffy, P. 2021, *ApJL*, 886, L26
- Silva, L. O., Fonseca, R. A., Tonge, J. W., Dawson, J. M., Mori, W. B., Medvedev, M. V., 2003, *ApJL*, 596, L121
- Sironi, L., Spitkovsky, A., Arons, J., 2013, *ApJ*, 771, 54
- Sironi, L. & Spitkovsky, A., 2014, *ApJ*, 783, L21
- Sironi, L., Petropoulou, M., & Giannios, D., 2015, *MNRAS*, 450, 183
- Spitkovsky, A., 2008a, *ApJL* 673, L39
- Spitkovsky, A., 2008b, *ApJL*, 682, L5
- Tchekhovskoy, A., 2015, *ASSL*, 414, 45
- Thum, C., et al. 2018, *MNRAS*, 473, 2506

- Uzdensky, D. A., 2011, *Space Sci. Rev.*, 160, 45
- Wardle, J.F.C., et al. 1998, *Nat*, 395, 457
- Wardle, J.F.C. & Homan, D.C., 2003, *Ap&SS*, 288, 143
- Weibel, E.S., (1959) 1959, *Phys. Rev. Lett.*, 2, 83
- Wendel, D. E., Olson, D. K., Hesse, M., et al., 2013, *PhPl*, 20, 2105
- Zenitani, S. & Hoshino, M., 2005, *ApJ*, 618, L111
- Zhang, B., 2018, *The Physics of Gamma-Ray Bursts*, Cambridge: Cambridge University Press.
- Zhang, B. & Yan, H., 2011, *ApJ*, 726, 90
- Zhdankin, V., Uzdensky, D. A., Werner, G. R., Begelman, M. C., 2018, *ApJL*, 867, L18

This paper has been typeset from a $\text{\TeX}/\text{\LaTeX}$ file prepared by the author.